Geochemistry, Geophysics, Geosystems®

AGU ADVANCING EARTH AND SPACE SCIENCE

RESEARCH ARTICLE
10.1029/2023GC010870

Key Points:

- The southern intra-transform ridge segment in the St. Paul transform fault system, over the last ~6 Myr is dominated by detachment faulting
- Several detachments have been split and partly transferred to the opposite ridge flank through ridge axis relocation
- The change in the accretionary processes, from Oceanic Core Complexes to mantle exhumation, suggests a decrease in the time of the melt supply

Supporting Information:

Supporting Information may be found in the online version of this article.

Correspondence to:

C. Vincent,
clementvincent@snu.ac.kr

Citation:

Vincent, C., Maia, M., Briais, A., Brunelli, D., Ligi, M., & Sichel, S. (2023). Evolution of a cold intra-transform ridge segment through oceanic core complex splitting and mantle exhumation, St. Paul transform system, Equatorial Atlantic. *Geochemistry, Geophysics, Geosystems*, *24*, e2023GC010870. https://doi.org/10.1029/2023GC010870

Received 24 JAN 2023
Accepted 22 APR 2023

Evolution of a Cold Intra-Transform Ridge Segment Through Oceanic Core Complex Splitting and Mantle Exhumation, St. Paul Transform System, Equatorial Atlantic

Clément Vincent[1,2], Marcia Maia[1], Anne Briais[1,3], Daniele Brunelli[4,5], Marco Ligi[6], and Susanna Sichel[7]

[1]Geo-Ocean, UMR6538 CNRS-IFREMER-UBO-UBS Institut, Universitaire Européen de la Mer IUEM, Brest, France, [2]Now at School of Earth and Environmental Sciences, Seoul National University, Seoul, South Korea, [3]Géosciences Environnement Toulouse—GET, Université Toulouse III—Paul Sabatier, Toulouse, France, [4]Dipartimento di Scienze Chimiche e Geologiche, Università di Modena e Reggio Emilia, Modena, Italy, [5]IGAG-CNR, Istituto di Geologia Ambientale e Geoingegneria, Rome, Italy, [6]ISMAR-CNR, Instituto di Scienze Marine, Bologna, Italy, [7]LAGEMAR, Universidade Federal Fluminense, Niteroi, Brazil

Abstract Accretionary processes at mid-ocean ridge segments with low magma input have seldom been investigated over the long term. The evolution of such magma-starved segments over time is still largely unknown. We present a study on the structure and evolution of the southernmost intra-transform ridge segment of the St. Paul Transform Fault System in the Equatorial Mid-Atlantic Ridge, based on new bathymetry, gravity, and rock sampling data. We show that this area evolves differently from previously described tectonics along ridge segments of similar spreading rate. On the flanks of the axial ridge segment, we observe a succession of structures exhumed by detachment faulting, evolving from east-facing, long-lived, corrugated oceanic core complexes (~6 Ma ago), to short-lived detachment faults exposing lower crust and mantle rocks and facing alternatively east and west in the more recent part of the segment. The oldest detachment faults have been repeatedly split and partially transferred to the opposite flank through the formation of new detachments into the footwall. The terminations of three old, east-facing detachments are observed on the east flank of the segment. The westward relocations of the plate boundary appear to compensate for the asymmetry of accretion through detachment faulting, overall creating the same amount of lithosphere on both flanks of the ridge. We interpret the observed changes in the time of the accretionary processes to reflect a decrease of the melt supply over the last ~6 Myr.

Plain Language Summary The generation of new seafloor at mid-ocean ridges where cold underlying mantle delivers low magma supply has not been investigated over the long term. Here we present the analysis of new bathymetry, gravity, and rock sampling data over such a ridge segment located within the St. Paul Transform Fault system in the Equatorial Mid-Atlantic Ridge, which allowed us to bring constraints on its structure and evolution over the last ~6 Myr. We show that this area evolves differently from previously described ridge segments of similar spreading rate. We observe the remnants of very large normal faults called detachment faults, which have been active for very long times, forming domes called oceanic core complexes. The fault surfaces have been dissected by further extensional deformation, until the plate motion became accommodated along a new detachment fault formed west of the previous plate boundary. The emergence lines of the detachment faults are observed on the eastern flank of the ridge segment. We also observe a change in time of the structures, from typical oceanic core complexes to shorter ridges formed by the exhumation of mantle rocks. We interpret these changes to possibly reflect a decrease in the melt supply in the last 6 Myr.

1. Introduction

At slow-spreading Mid-Ocean Ridges (MOR) like the Mid-Atlantic Ridge (MAR) (full spreading rate: 20–40 mm/yr), axial magmatism and tectonics result in an overall symmetrical creation of new oceanic crust. In the last decades, however, a growing body of evidence has attested for asymmetric spreading at the segment scale (e.g., Escartin et al., 2008). These regions are commonly characterized by large-offset low-angle normal faults (several km) exposing deep crustal and mantle rocks on one side of the ridge axis facing hummocky volcanic terrains and smaller-offset normal faults on the opposite side (e.g., Blackman et al., 1998; Cann et al., 1997; MacLeod et al., 2009; Smith et al., 2006, 2008; Tucholke et al., 1998). Numerical models show that these

large-offset detachment faults develop when tectonic extension equals or dominates over magmatic spreading (Buck et al., 2005; Olive et al., 2010; Tucholke et al., 2008). When the fraction of total plate separation rate accommodated by dyke opening (factor *M*, Buck et al., 2005) remains between 0.5 and 0.3 for several millions of years, long-lived detachment faults form structures named Oceanic Core Complexes (OCCs) in analogy with continental metamorphic core complexes (e.g., Blackman et al., 1998, 2011; Cann et al., 1997; Dannowski et al., 2010; Dick et al., 2008; Smith et al., 2006, 2008). OCCs are characterized by domed and smooth surfaces delimited by a termination and a breakaway. The detachment breakaway marks the initiation of the long-lived fault and is often visible as a linear ridge oriented parallel to the axial valley (Blackman et al., 1998, 2009; Cann et al., 1997; Escartín et al., 2017, 2022; Smith et al., 2006; Tucholke et al., 1998). The termination of an OCC is the line of emergence of the detachment fault from the hanging wall, often showing an irregular accumulation of rubbles forming an apron (Escartín et al., 2017). It usually appears as a sharp line separating the rough seafloor, associated with the hanging wall volcanic terrains and the apron, and the smooth footwall surface. In most cases, the detachment faults of OCCs present corrugations or striations parallel to the spreading direction. The corrugations and striations represent the traces of the fault slip, possibly due to irregularities in the hanging wall or in the brittle-plastic transition at depth, or localization of brittle deformation on a network of linked fractures (Blackman et al., 1998, 2009; Cannat et al., 2009; Ildefonse et al., 2007; MacLeod et al., 2002; Parnell-Turner et al., 2018; Reston & Ranero, 2011; Smith et al., 2006; Spencer, 1999; Tucholke et al., 1998, 2008). OCCs are active for roughly 1–3 Myr (e.g., Tucholke et al., 1998, 2008) up to about 4 Myr for Godzilla Megamullion (Ohara et al., 2001; Tani et al., 2011) which is an exceptionally long-lived detachment, yet, the long-term temporal evolution (up to 5–6 Myr) of OCC-bearing ridge systems has not been fully explored to date. Areas where the magmatic input is even lower or absent (*M* under 0.3) display a "smooth seafloor" morphology formed by ridges of exhumed peridotite with eroded fault scarps and no corrugations (Cannat et al., 2006, 2019; Olive et al., 2010; Sauter et al., 2013; Tucholke et al., 2008).

Here we discuss the morphology and structure of the southern intra-transform ridge segment of the St. Paul transform system in the Equatorial MAR. The ridge flanks show features characteristic of areas of low melt supply described on the flanks of other segments of the MAR or in other mid-oceanic ridges. We use the seafloor morphology and backscatter data, combined with gravimetry and rock sampling, to explore the temporal evolution of the structures on conjugated ridge flanks. Our study provides constraints on the long-term evolution of seafloor spreading in a particularly magma-starved slow-spreading segment.

2. Tectonic Context and Study Area

The Equatorial Atlantic is characterized by the presence of major transform faults (Figure 1a), which offset the axis of the MAR by several hundreds of kilometers. The large-offset Romanche and St. Paul transforms (~900 and 570 km cumulative offsets, respectively) are among the largest of the MOR system. These mega-transforms (Ligi et al., 2002) appear as complex, multi-fault plate boundaries where the transform domains extend for more than 100 km and show evidence for intense intra-transform tectonics and magmatism (Hekinian et al., 2000; Ligi et al., 2002; Maia et al., 2016).

The Equatorial MAR has long been interpreted as a "cold spot" in the MOR system, that is, associated to a regional low of the sub-axial mantle temperature (Bonatti, 1990; Bonatti et al., 1993; Schilling et al., 1995). Supporting pieces of evidence are the very deep axial and transform valleys (>5,000 m and up to ca. 8,000 m, respectively) reaching near the Equator the largest depths of the whole MAR. Overall, the ratio of mantle-derived peridotite to basalt sampled in the region is high, with large areas of the ocean bottom floored by abyssal peridotites showing lower degrees of melt extraction (<5%) compared to other sections of the MAR (Bonatti et al., 1993, 2001; Brunelli & Seyler, 2010; Hekinian et al., 2000; Schilling et al., 1995). These observations suggest that the melting regime in the Equatorial Atlantic is lower than the world average, due either to colder than average mantle temperatures or to an anomalous composition of the mantle source compared to other MAR segments (Bonatti et al., 1993, 2001; Schilling et al., 1995; Seyler & Bonatti, 1997; Sichel et al., 2008). The chemical composition of basalts and peridotites sampled in the equatorial region presents a marked enrichment in incompatible elements implying compositional anomalies in the sub-ridge mantle (Bonatti, 1990; Bonatti et al., 1993; Esperança et al., 1999; Hekinian et al., 2000; Schilling et al., 1995; Sichel et al., 2008) or an extreme contraction of the melting region above the hydrous solidus in the garnet facies (Bonatti et al., 2001; Brunelli & Seyler, 2010; Ligi et al., 2005).

10.1029/2023GC010870

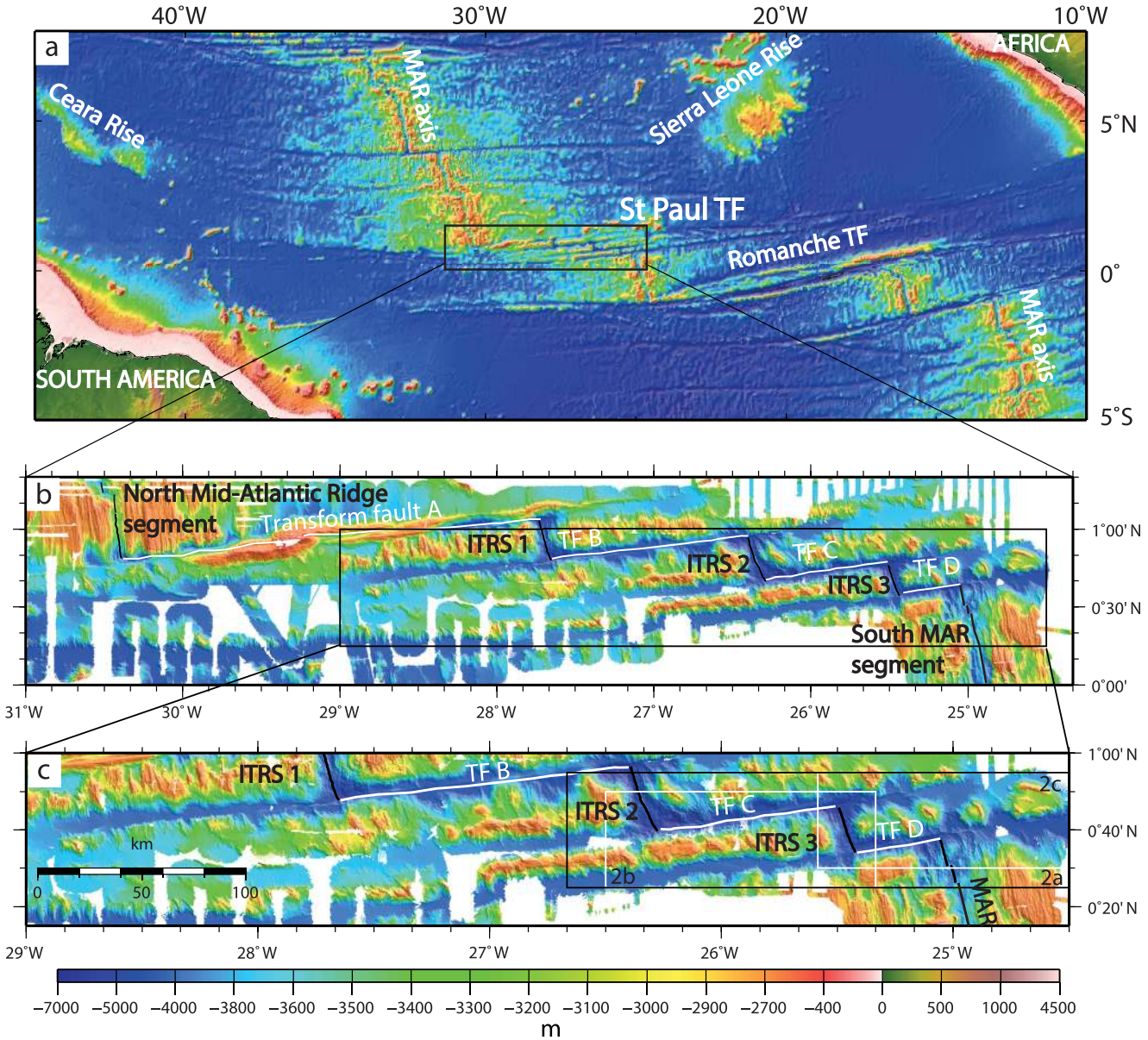

Figure 1. Shaded bathymetric maps of the Equatorial Atlantic. (a) Location of the study area and main tectonic features of the Equatorial Atlantic (Smith & Sandwell, 1994). TF, Transform fault; MAR, Mid-Atlantic Ridge; (b) Bathymetry of the St. Paul transform fault system. ITRS, Intra-Transform Ridge Segment; (c) Bathymetry of the southern intra-transform segment. The black and white boxes represent the boundaries of Figures 2a–2c. White lines are transform faults. Black lines show ridge axis (b and c bathymetry from Maia et al. (2014)).

The St. Paul transform system (Figure 1b) is formed by four Transform Faults (TF, A–D from North to South, respectively) offsetting the MAR axis and three Intra-Transform Ridge Segments (ITRS, 1–3 from North to South). The ITRSs do not exceed 25 km in length and display a typical hourglass shape, with a narrow axial valley in their central part, 4,600–4,700 m deep, and a wider and deeper (>5,000 m) valley at their ends. Ridge offsets progressively decrease from TF A (297 km)–TF B (142 km), TF C (90 km), and TF D (~47 km). In this paper, we focus on the southernmost intra-transform ridge segment of the system, ITRS 3, centered at 0°39′N, 25°28′W. This segment is bounded by TF C and TF D, the latter representing the southern boundary of the entire St. Paul system (Figure 1c).

Early sampling and submersible studies of the St. Paul ITRS 3 axial area revealed an abundance of serpentinized peridotites and a thin cover of basalts not exceeding 150 m, suggesting an accretion process involving mantle exhumation associated with weak and sporadic magma supply (Hekinian et al., 2000). The volume of

10.1029/2023GC010870

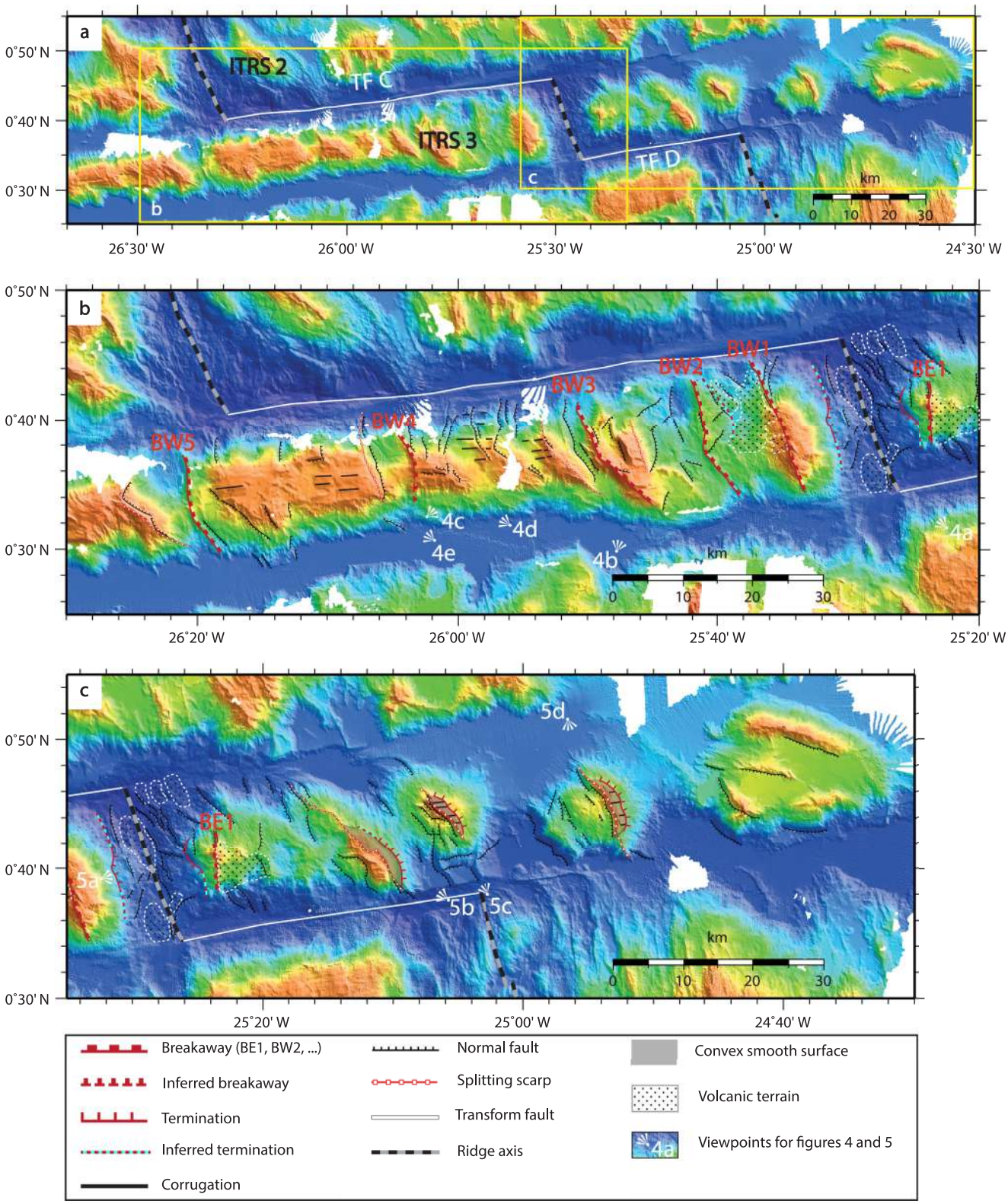

Figure 2. Structural maps of the St. Paul ITRS 3. (a) Shaded bathymetric map of the segment showing the frames of this Figure (2b and 2c). (b) Detailed map of the structures on the western ridge flank. (c) Detailed map of the structures on the eastern ridge flank. The color scale is the same as in Figure 1. The different viewpoints correspond to the 3D views in Figures 4 and 5.

basaltic rocks estimated by Hekinian et al. (2000), based on dyke occurrence and observed lava flows, is approximately 1/3 of the estimated "normal" magma productivity at slow-spreading ridges (10^{-5} km^3/year per km of ridge, Hekinian et al., 2000). The small amount of melt delivered to the crust suggests a major role of tectonics, and the possible development of long-lived detachment faults (MacLeod et al., 2009; Smith et al., 2006). The recent exploration of the St. Paul region during the COLMEIA cruise (Maia, 2013; Maia et al., 2014, 2016, 2017) showed that the magma supply differs significantly between the three intra-transform ridge segments. While the northern ITRS 1 has a volcanic crust, with clear fault-bounded abyssal hills (Maia et al., 2014, 2016), the central and southern ITRSs 2 and 3 appear to be magma-starved, characterized by large OCCs mainly located on the west flank of the ridge, and broad and smooth large abyssal hills likely formed by peridotite ridges. Abundant gabbros and serpentinized peridotites, frequently mylonitized, were sampled on their flanks (Maia et al., 2014, 2016).

The geochemical isotopic signature of the basalts suggests the existence of a mantle compositional boundary inside the St. Paul system (Schilling et al., 1995). An enriched mantle endmember attests to the interaction of the Sierra Leone plume with the Mid-Atlantic Ridge segment north of the St. Paul system. Its influence extends to ITRS 1 (Le Voyer et al., 2015; Schilling et al., 1994, 1995). The morphology of these ridge segments reflects a vigorous volcanic activity possibly resulting from the combination of higher source fertility with higher potential temperature of the sub-ridge mantle (Maia et al., 2016). In contrast, ITRS 3 is spreading over a colder mantle, and geochemically similar to that sampled near the Romanche transform, south of St. Paul (Schilling et al., 1995).

3. Data and Methodology

During the COLMEIA cruise onboard the RV L'Atalante (Maia, 2013; Maia et al., 2014, 2017) in January–February 2013, we acquired new bathymetry, multichannel seismic and gravity data as well as rock samples in the St. Paul multi-transform system.

3.1. Multibeam Bathymetry

The bathymetric mapping used the Kongsberg EM122 multibeam echosounder, mostly in dual mode swath, at 10 knots, which ensured a high-density sampling over an angular coverage of 140°. The bathymetric precision is about 0.2% of the water depth, that is, ca. 6 m at depths of 3,000 m. Multibeam data processing was carried out on board using the CARAIBES software (©Ifremer). The EM122 bathymetric data were then combined to the data acquired during the previous cruises PRIMAR96 and S7 of RV Strakhov (Gasperini et al., 1997; Udintsev, 1996) to generate grids at resolutions of 50 and 100 m.

The identification of the faults and main structural features was made on bathymetric, backscatter, and slope maps, and 3D views, complemented by the gravity-derived crustal thickness map, rock sample characteristics, and observations from submersible in Hekinian et al. (2000). The main tectonic features were drawn and digitized using QGIS (QGIS.org, 2022. QGIS Geographic Information System. QGIS Association. http://www.qgis.org), Global Mapper® and GLOBE (Poncelet et al., 2022) softwares (Figures 2–6). We interpreted the relatively linear steep scarps as high-angle normal faults. The detachment faults were identified from large, domed surfaces sometimes showing corrugations. Breakaways were often difficult to identify because of the heavy mass wasting. In a few places, deep crustal or mantle rocks (gabbro, peridotite and serpentinite) have been dredged (dredges COL-DR26, COL-DR27, COL-DR28, COL-DR30, and COL-DR31, Figure 3a), supporting the morphological identification of detachment faults. In the distal parts of the study area, flat basin morphologies correspond to areas where the structures are covered by a blanket of sediments. Sedimentation rates in the Equatorial Atlantic ranged between 0.6 and 1.7 cm/Kyr over the past 10 million years (Wagner, 2002). The analysis of existing seismic profiles (Gasperini et al., 1997; Maia et al., 2014, 2017) confirms that, except in the deepest basins, the thickness of the sediments is lower than 50 m (see Section 3.3), making it possible to identify most structural trends. We interpret as volcanic the structures characterized by rough and hummocky morphology, or sometimes showing individual seamount conical shapes, and often confirmed by the presence of basalts in the associated dredge hauls (e.g., dredge COL-DR29, Figure 3a) or dive observations and sampling. Parts of the axial valley floor where basalts have been observed (submersible dive SP1 Figure 3a; Hekinian et al., 2000) present a smooth and homogeneous morphology on the bathymetric and reflectivity maps (Figures 2 and 4a and Figure S1 in Supporting Information S1), suggesting that interpretation of volcanic domains from bathymetry data alone is difficult. Hence, we prefer to name these zones "smooth undetermined area" when the absence of ground truthing prevents us to identify the lithology (Figures 3–6).

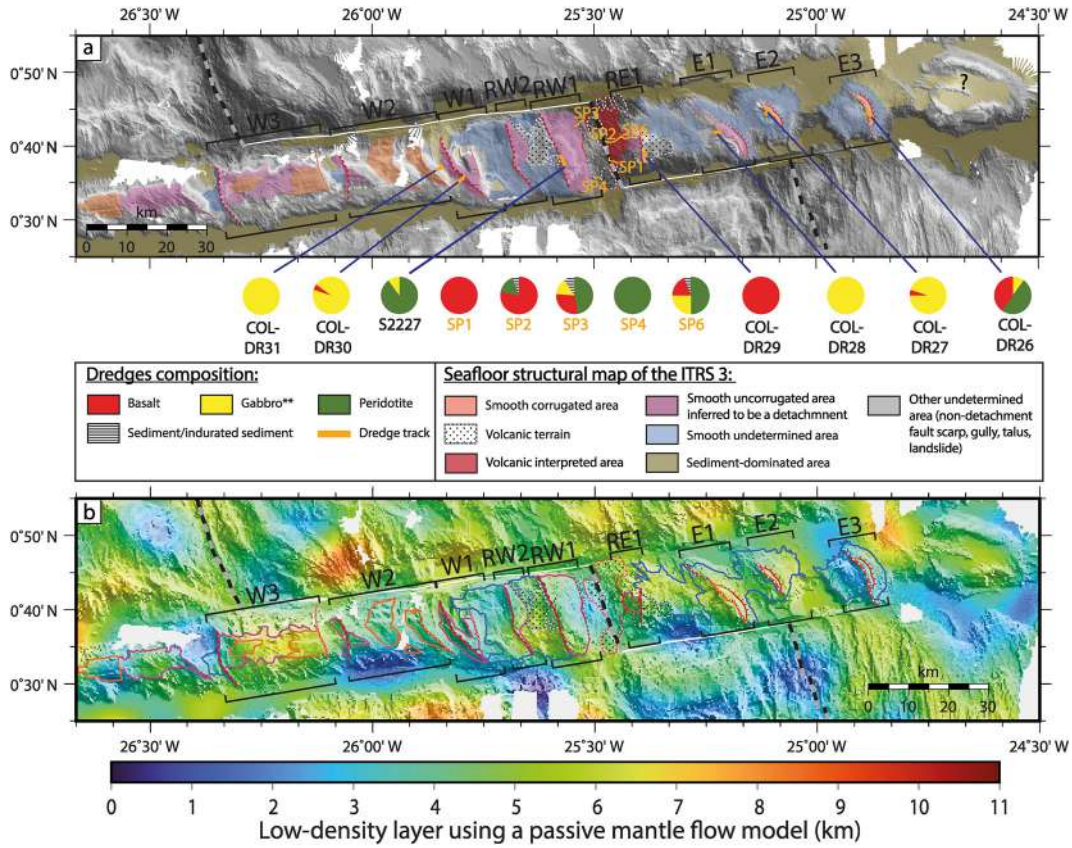

Figure 3. (a) Composition and location of the dredges and dives carried out on the St. Paul ITRS 3. The location and composition of the dredge S2227 are from D'Orazio et al. (2004). The numbered pink lines (SP) indicate the different dive tracks undertaken with the NAUTILE submersible (Hekinian et al., 2000). Symbols of the main structures as in Figure 2. (b) Map of the low-density layer (LDL) thickness (2,800 kg/m³) estimated from the inversion of the residual Mantle Bouguer gravity anomaly estimated using a passive mantle flow model. The main tectonic structures are represented and the symbols are as in Figure 2. The main seafloor structural information interpreted from the bathymetry, petrology and gravity data are draped on the two maps. Volcanic terrain corresponds to area where volcanic features are clearly identified. Volcanic interpreted areas represent areas where no morphological evidence of volcanism (like cones, hummocky seafloor…) is observed but where the backscatter, LDL thickness and dives observations (Hekinian et al., 2000) suggest a volcanic seafloor. The smooth undetermined areas correspond to areas with a smooth morphology where no clear characteristics of a detachment fault are observed or where no outcrop samples are available. These areas may correspond to smooth volcanic or exhumed terrains.

3.2. Rock Samples

During the COLMEIA cruise, six sites were successfully dredged on the flanks of the ITRS 3 (Maia, 2013; Maia et al., 2014, 2017): two dredges on the west flank (South American plate: COL-DR30 and COL-DR31) and four on the east flank (Nubian plate: COL-DR26 to COL-DR29, Figure 3). Dredges COL-DR30 and COL-DR31 collected only gabbroic rocks compositionally ranging from olivine-bearing to oxide gabbro. Overall, these samples attest to a multistage magmatic history recorded by extreme grain size variability at the sample scale ranging from micro- to very coarse-grain textures. Several leucocratic and oxide-rich veins and patches are also present attesting to intrusions of markedly evolved melts in cooling crystal mush (Brunelli et al., 2020). Magmatic textures are locally overprinted by ductile deformation. Fractures are sealed by chlorite and serpentine veins. Dredges from the eastern side recovered a wide variety of lithologies: COL-DR29, located on the wall of the axial valley, recovered large amounts of fresh basalts pertaining to at least two different extrusions. They present fresh glassy rims, and texturally range from aphyric to Pl-phyric and minor Pl-Ol-phyric. Eastward, only one large block of isotropic, coarse-grained, olivine gabbro was recovered in dredge COL-DR28. The two easternmost dredges COL-DR27 and COL-DR26 recovered few altered aphyric basalts along with pervasively deformed gabbros and serpentinites. The latter recorded intensive deformation under variable P-T conditions

10.1029/2023GC010870

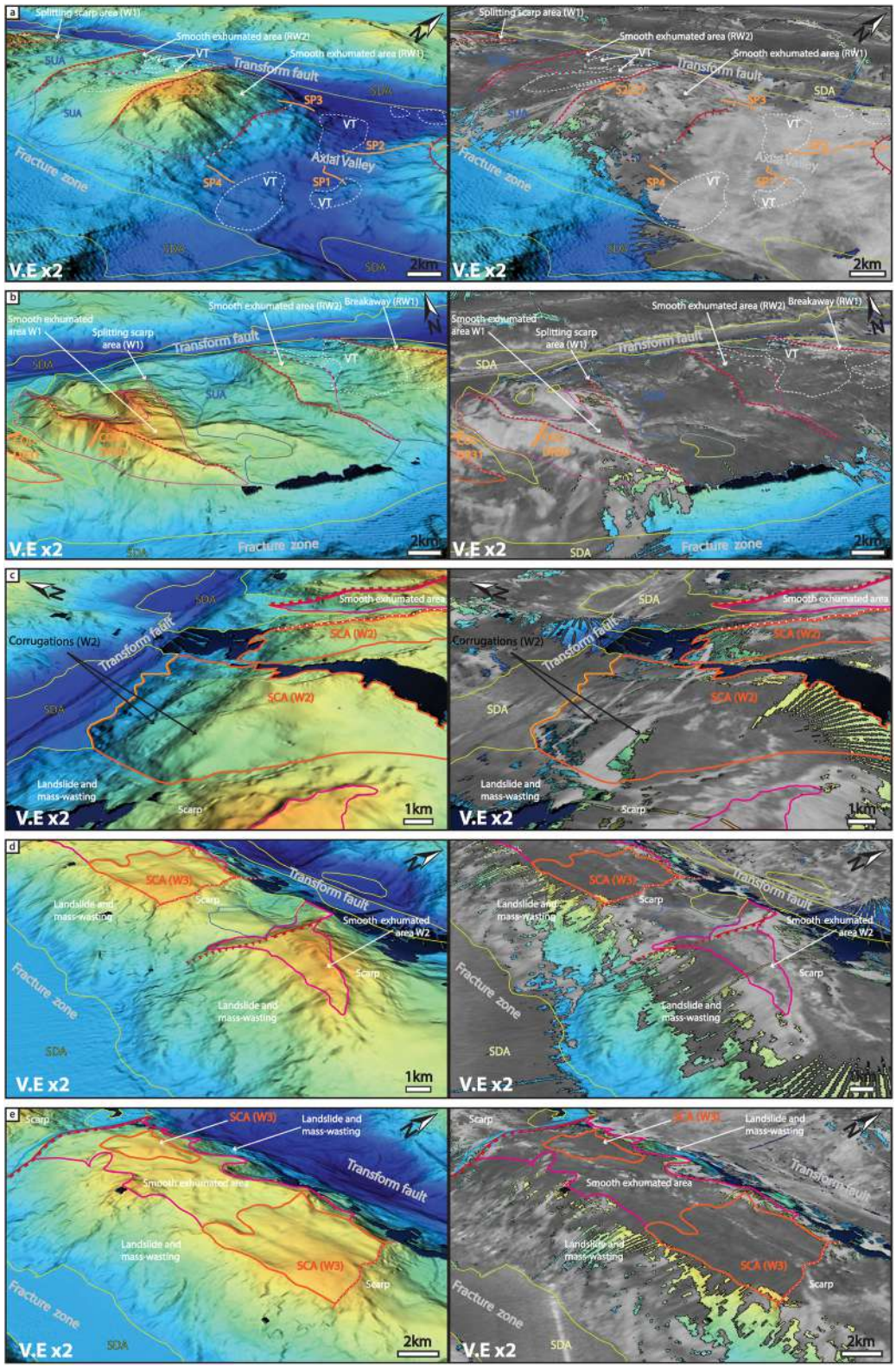

Figure 4.

leading to extensive mylonitization of both gabbros and serpentinites. Gabbroic rocks record ductile deformation under anhydrous conditions. Locally, cm-thick ultramylonitic shear bands are present, marked by strong grain size reduction and sub-mm scale pervasive foliation. Instead, serpentine mylonites show evidence of deformation after hydration which completely overprints the protolith textural characters. Although not all tectonic features of the area were sampled, these dredges attest for large exposures of deep rocks and reveal the lithological variability of the south intra-transform segment of the St. Paul system. We use the shipboard sample descriptions and classifications to constrain the structural interpretations. Chemical analyses of these samples are under way and will be discussed in a forthcoming paper.

3.3. Gravity Data Processing and Modeling

Gravity data were collected along the ship tracks using a Bodenseewerk KSS30 gravimeter at a sampling interval of 10 s. Data were processed in the conventional way, by averaging and filtering the measurements to remove the noise and applying the Eotvös, drift and latitude corrections to obtain the free air anomaly. The modeling procedures are detailed in Supporting Information S1 and illustrated in Figure S2 of the Supporting Information S1. Due to the irregular spacing of the ship tracks, shipboard data were merged with the free air anomalies computed from altimeter data (Sandwell et al., 2014), yielding a complete grid that retains the high frequencies of the shipboard anomalies (Maia & Arkani-Hamed, 2002; Figure S2a in Supporting Information S1). The density model used herein consists of three layers of constant density: sediment cover, crust or altered mantle (or their density proxy) and the normal mantle, respectively, with densities of 1,500, 2,800, and 3,300 kg/m^3. Water density was set at 1,030 kg/m^3. The low-density value chosen for the sediments is consistent with the results of Tenzer and Gladkikh (2014). The sediment thickness grid (Figure S2b in Supporting Information S1) was built based on values derived from the interpretation of the seismic lines obtained during the COLMEIA cruise as well as data derived from seismic lines acquired on previous cruises (Gasperini et al., 1997; Maia, 2013; Maia et al., 2014, 2017). Most of the studied area presents a relatively thin sediment cover (less than 50 m), except for some localized areas. The sedimentary infill reaches a maximum of 790 m only in the basins associated with the older sections of the fracture zones, decreasing to ∼200 m in the nodal basins. For the gravity model, we interpolated the high-resolution bathymetry onto a UTM projected grid at a resolution of 1 km compatible with the final resolution of the sediment thickness grid. The basement topography was obtained from the bathymetry and the sediment thickness grids (Figure S2c in Supporting Information S1). To calculate the Mantle Bouguer anomaly (Figure S2d in Supporting Information S1), we assumed a constant, 6 km-thick "volcanic crust" (or its proxy, a 2,800 kg/m^3 density layer), using the basement as the top of the layer. The final model covers the entire St. Paul system, and to prevent edge effects on the calculation, we included a lower resolution larger area in the grids used for the model. The gravity effect of this model was computed in the Fourier domain using the multi-layer method, developed to account for both rapidly varying topography and shallow water depths, and subtracted from the free-air anomaly grid yielding the Mantle Bouguer anomaly (Maia & Arkani-Hamed, 2002). We then proceeded to remove the effect of lithosphere cooling by testing two different thermal models: a simple plate cooling model based on lithospheric ages (Parsons & Sclater, 1977; Stein & Stein, 1992), and a passive flow model (Ligi et al., 2008; Morgan & Forsyth, 1988) using 1 mm^2/s for the thermal diffusivity and 2.7×10^{-5} °C^{-1} for the thermal expansion coefficient. Our calculations show that the different thermal settings result in minor differences between models (Figures S2e and S2f in Supporting Information S1), which appear mostly as a broad regional trend, and therefore we chose to retain the passive flow model (see Supporting Information S1 for a full discussion of this topic). The resulting residual Mantle Bouguer anomaly (RMBA, Figure S2h in Supporting Information S1) was then inverted to yield variations of the thickness of the 2,800 kg/m^3 layer or "low-density layer" (LDL), which were added to the assumed 6 km-thick layer (Figure 3b and Figure S2j in Supporting Information S1).

Figure 4. Perspective views of the five most significant structures observed of the west flank of the St. Paul ITRS 3. The left panels correspond to the bathymetry images and the right panels correspond to the reflectivity images. (a) 3D view of RW1and RW2, the smooth ridges closest to the axis. The absence of corrugations and the presence of numerous gullies make it difficult to identify the fault terminations. Scarce volcanic terrain is identified in the axial valley and between RW1 and RW2 (b) 3D view of the W1 breakaway (BW3) and the ridge (RW2) closer to the axial valley. We note that W1 does not show any corrugations and that the two sides of the breakaway of W1 are smooth. The splitting scarp represented by a structural discontinuity is also visible. (c) 3D view of the fractured W2, a smooth detachment surface with corrugations. (d) 3D view of BW4, the breakaway of W3. Numerous scarps, landslides and mass wasting are observed but no clear corrugation is observed on this section of W2. (e) 3D view of W3, with a fine example of smooth exhumed surface with well-marked corrugations. All perspective projections have been realized with GLOBE software (Poncelet et al., 2022). See Figure 2b for the locations of the different viewpoints. The abbreviations correspond to: Volcanic Terrain (VT, the white dotted line area); Smooth Undetermined Area (SUA, the blue line area); Smooth Corrugated Area (SCA, the orange line area); Sediment-Dominated Area (SDA, the yellow line area); V.E (Vertical Exaggeration).

10.1029/2023GC010870

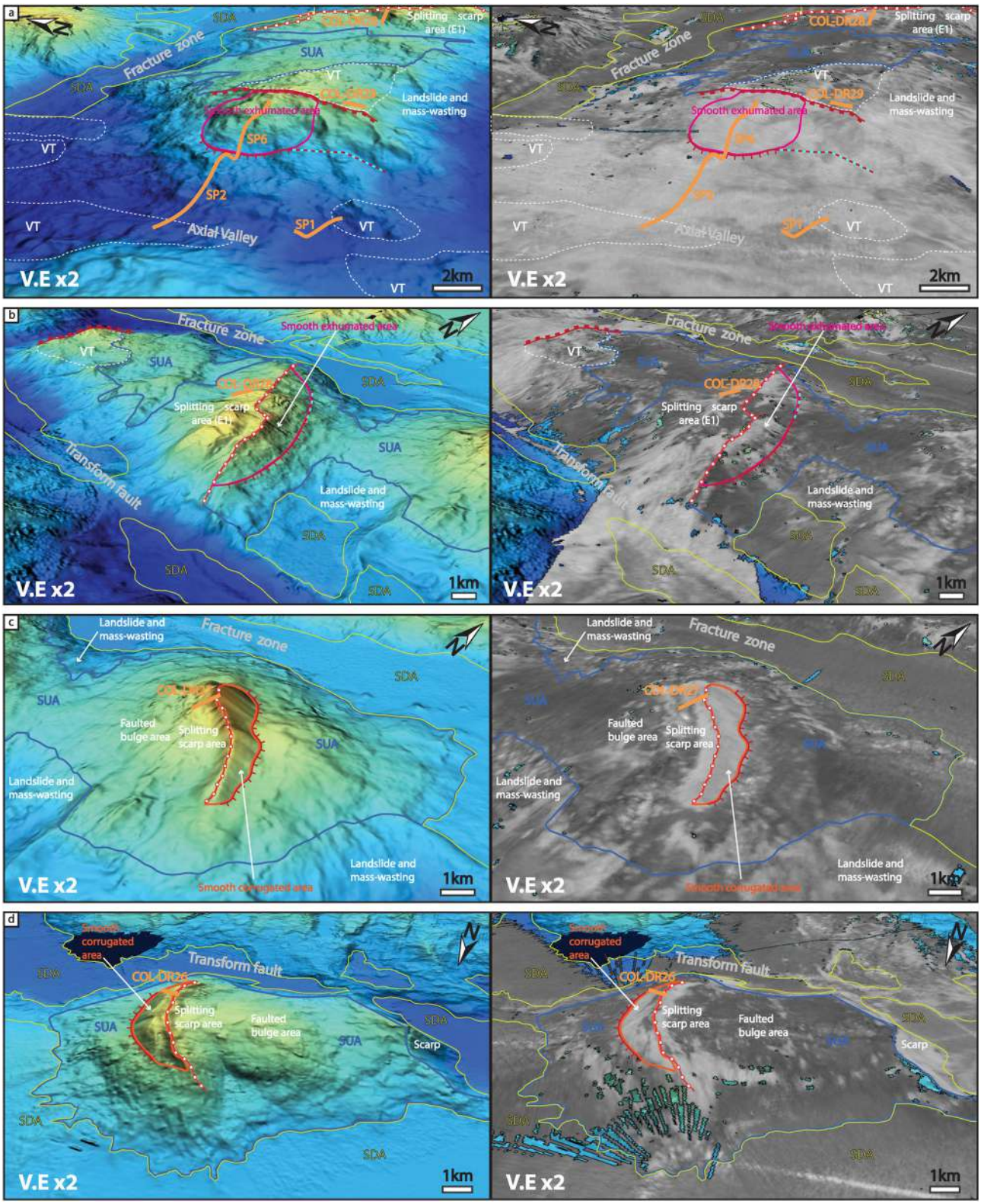

Figure 5.

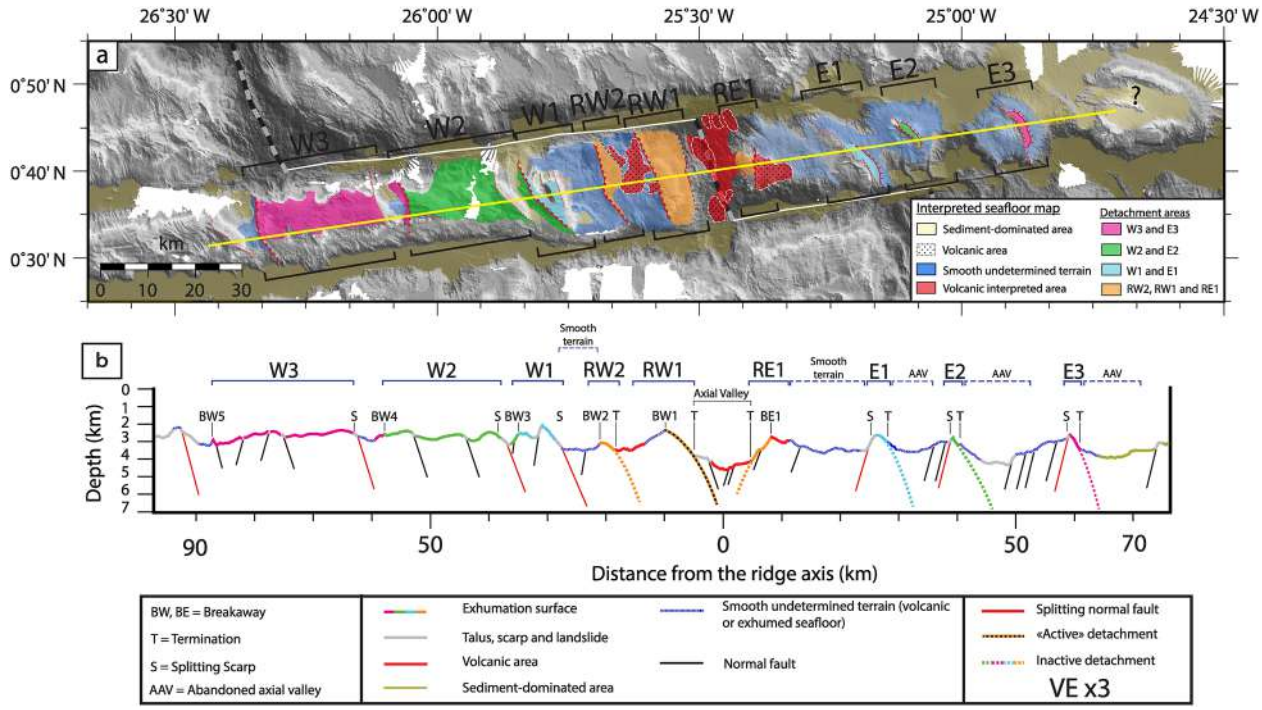

Figure 6. (a) Summary of interpreted tectonic/structural features on shaded bathymetry map. The color scale is the same as that in Figure 1. Symbols of the main structures as in Figure 2. Volcanic terrain corresponds to area where volcanic features are clearly identified. Volcanic interpreted areas represent areas where no morphological evidence of volcanism (like cones, hummocky seafloor…) is observed but where the backscatter, LDL thickness and dives observations (Hekinian et al., 2000) suggest a volcanic seafloor. The yellow line represents the location of the cross section in the bottom inset. (b) Interpretative cross section showing the large structures of the St. Paul ITRS 3 based on bathymetry, sampled rocks and gravity data (see text). The different surfaces colored in orange, blue, green and pink delimit the detachment surfaces. The corresponding split portions of the detachment with terminations are drawn with the same colors on the eastern side. The black lines mark normal faults. The splitting normal faults represented in red are the normal faults closest to the structural splitting scarp (S). In this figure and following, we adopt a detachment fault dip of 60° below the anchoring point (Anderson, 1951; MacLeod et al., 2009; Reston & Ranero, 2011; Schoolmeesters et al., 2012) VE: Vertical Exaggeration (here X3).

Gravity model results should be interpreted with caution because of the short-scale lateral variability in both morphology and lithological occurrences. The 2,800 kg/m^3 density usually corresponds to basalt and gabbro but may also reflect altered and serpentinized peridotites, as well as mylonites and other altered lower crustal rocks. We emphasize that the gravity analysis yields a simplified image of the oceanic crust and mantle. Structural and petrological variabilities along a detachment result in heterogeneous gravity signatures. It is therefore necessary to use morphological and petrological observations (when available) to correctly interpret the gravity analyses. Moreover, additional uncertainties in the gravity model may arise from local effects and from a simplified thermal model that does not consider the complex evolution of the spreading processes through time (see further discussion in Text S1 and Figure S2 of the Supporting Information S1).

4. Structure of the Southern St. Paul Intra-Transform Ridge Segment and Its Flanks

The compiled multibeam bathymetry covers the southern intra-transform ITRS 3 segment of the St. Paul transform system up to about 29°W to the west, and 24°30′W to the east.

The westernmost part of the segment reveals oblique ridges trending NW-SE between ~28°30′W and 27°W, and a single, 75-km-long, 10-km-wide corrugated surface in the northern half of the segment between 27°W

Figure 5. Perspective views of four structures of the east flank of the St. Paul ITRS 3. The left panels correspond to the bathymetry images and the right panels correspond to the reflectivity images. (a) 3D view of RE1, the ridge closest to the axis. The flat and smooth undetermined area (SUA) between RE1 and E1 is visible, as well as limited volcanic terrains (VT) in the axial valley. (b) 3D view of the first off-axis ridge E1. No corrugation is visible on this smooth convex flank toward the east. Its splitting scarp is characterized by the ridge line overhanging the steep west-facing flank. The abandoned axial valley separating E1 and E2 is also observable. (c) 3D view of the ridge E2, interpreted to be the termination side of OCC2. We note the steep dip of the convex flank, which appears smooth and corrugated. (d) 3D view of the ridge E3. All perspective projections have been realized with GLOBE software (Poncelet et al., 2022). See Figure 2c for the locations of the different viewpoints. Same abbreviations as in Figure 4.

and 26°33′W (Figure 1c). The long, corrugated surface reaches depths of only 2,000 m in some points and its eastern end near 26°33′W is marked by a scarp affected by several large landslides (Figure 2). Between 26°33′W and 26°20′W, eroded ridges oblique to spreading are also bounded to the east by a large scarp. This morphology reveals that spreading along the segment was accompanied by oceanic core complex formation between about 10 and 6 Ma. We compare the structures on the west flank with the conjugate structures on the east flank to constrain the evolution of the accretionary processes in the last ~6 Myr. Because we do not have enough information (e.g., rock samples) about the older area and the potential conjugate part to the east (~24°40′W), we focus on the structures between 26°20′W and 24°47′W, which are discussed in the following paragraphs.

In the studied area, the seafloor morphology of both flanks presents a sequence of prominent flat or domed, long and smooth surfaces, as well as smaller structures characterized by broad, smooth and rounded ridges or massifs (Figures 1 and 2). Numerous fragments of smooth surfaces free of volcanic cones typical of detachment footwalls (Figure 2) show undulations of variable width, elongated parallel to the spreading direction, which we interpret to be corrugations of long-lived detachment faults (OCC). However, the corrugated surfaces observed on the western ridge flank do not show the termination geometry and terrain roughness contrast at the base of typical detachment surfaces or at breakaways. Instead, they are interrupted by large high-angle normal faults, and narrow and smooth basins. Features showing a "termination" morphology are instead present on the opposite, eastern flank. Also, most of the ridges and massifs observed on both flanks show an oblique orientation with respect to the transform faults or fracture zones. Only the most recent structures appear to be perpendicular to spreading.

Volcanic constructions are very rare. We observe clear volcanic zones characterized by rough terrains, hummocky ridges and conical volcanoes (Figure 2) associated to a high backscatter (Figures 4 and 5; Figure S1 in Supporting Information S1), only in few places, close to the present-day axial valley and in the valley itself. Samples confirm the volcanic nature of some of these units (Hekinian et al., 2000; Maia et al., 2014; Schilling et al., 1994, 1995).

Mass wasting features and erosional gullies are also frequently observed on the flanks of all bathymetric highs, sometimes making it difficult to identify the original structures. These features have variable dimensions, and some are similar to subaerial or other submarine landslides (Cannat et al., 2013; Tucholke, 1992). These remobilized areas are characterized by high reflectivity, and often contrast with homogeneous, low backscatter and smooth areas corresponding to the exhumation surfaces (Figures 4 and 5).

4.1. Ridge Axis Morphology and Structure

The 23 km-long axis of the southern intra-transform segment extends from 0°34′N to 0°46′N around 25°28′W (Figures 1 and 2). The rift valley has a narrow hourglass shape, about 4,500 m deep in its central part, becoming wider and deeper toward the segment ends where large nodal basins reach 5,200 m in depth to the north, and 4,850 m to the south. Across axis, the topographic relief between the rift shoulders and the axial floor is about 1,600 m, larger than the average of the segments of the MAR between 15°N and 37°30′N (Thibaud et al., 1998). The axial valley floor is characterized by the brightest reflectivity, highlighting recent volcanics, scarps and talus (Figures 4a and 5a; Figure S1 in Supporting Information S1). The spreading axis is located near the center of the axial valley and near the eastern wall toward the segment southern end, with sparse hummocky terrain and individual volcanoes observed in the deepest parts of the axial valley (Figures 2, 4, and 5; Figure S1 in Supporting Information S1). During submersible dives (see locations on Figure 3a), Hekinian et al. (2000) observed a series of active fissures oriented N340° and N-S, disrupting a thin sedimentary cover, and glassy lava flows on the valley floor at the base of the east wall, confirming that recent volcanic structures are present on the eastern part of the axial valley. They concluded that the volcanic activity is weak and sporadic, producing only small volumes of lava. The gravity-derived LDL is thinner than the 6 km average, with values ranging from 4.3 to 5 km below the northern and the southern nodal basins, respectively, and 2.8 km in the central part of the axial valley (Figure 3b). This unusual LDL pattern is discussed later.

The eastern wall of the axial valley consists of a dome-shaped bathymetric high affected by west-dipping normal faults oriented N140–150°E, N-S, and N110°E, and by mass-wasting (Figures 2b and 5a). The normal faults in the northern part of the segment are more numerous than those in the south. These faults do not form a pattern of linear, ridge-parallel abyssal hills. The bathymetric dome, called RE1, is topped by an axis-parallel ridge that culminates at ~2,700, 1,900 m above the axial valley floor. Conical seamounts are observed in the northern part of the structure (Figures 2c, 5a, and 5b). The samples dredged at the southern top of the east valley wall (COL-DR29) are mostly fresh glassy basalts (Figure 3a). During a submersible dive on the east valley wall near the center of the segment, Hekinian et al. (2000) observed basaltic rocks, pillows and doleritic dykes exposed

along faults in the upper part of the section, but also peridotites, associated with basalt and doleritic dykes, as well as gabbroic veins, often associated with normal faults, in the middle part of the slope. These observations suggest the presence of a thin basaltic layer, not exceeding 150 m, overlying deeper crustal and mantle rocks (Hekinian et al., 2000). This thin basaltic area does not present any well-defined seamount or volcanic structure but does show a high reflectivity (Figure 5a). The eastern valley wall is less homogenous than the smooth and domed slope on the western flank of the axial valley. The results of the gravity inversion suggest a thickness between 4 and 6 km for the LDL. The LDL is thin where peridotite and gabbro have been observed, and slightly thicker in the northern part of the valley wall. This gravity signature can be generated by either crustal material or serpentinized mantle, underlying this bathymetric high. Based on seafloor morphology, the nature of the dredged samples and dive observations, we interpret the near-normal RE1 LDL thickness as resulting from the contribution of altered, mantle-derived peridotites covered by a thin layer of magmatic crust. We posit that the ridge RE1 likely results from the displacement along a west-facing detachment fault, which uplifted the volcanic terrain formed at the ridge axis and now observed along the breakaway BE1 (red thick dashed line in Figures 2, 3, 5, and 6). The RE1 termination is located at the bottom of the smooth domal surface (TE1, ~25°26′W), is covered by mass wasting and recent volcanics, and affected by numerous normal faults (Hekinian et al., 2000).

The western valley wall has a smoother slope than the eastern wall and forms the side of a broad and rounded ridge, RW1, which extends over the entire length of the segment and reaches 2,400 m above the axial valley (Figures 2b, 3, and 4a). The ridge culminates at 2,140 m depth and is oriented N160°E. Nautile dives and near-bottom videos from the northern axial valley wall, close to the ridge-transform intersection (RTI) and on the southern part of the wall, show abundant peridotite outcrops mixed in some places with a thin basaltic layer (Figure 3a) (Hekinian et al., 2000). Some small areas of rough terrain, interpreted to be volcanic, are observed west of the ridge crest in the bathymetry, and outcrops of peridotite and gabbro with a thin or absent sedimentary cover have also been observed by a deep-towed camera survey on the western flank of RW1 (SCAMPI 09, D'Orazio et al., 2004 from R. Hekinian & B. Sichler, Personal Communication; Hekinian & Juteau, 1997). The thickness of the gravity-derived LDL ranges from 2.8 to 5.5 km, with the thinnest areas located on the east flank of the structure and the thickest on its southwest flank (Figure 3b). The area of thinner LDL extends into the axial valley floor in the center of the segment and corresponds to the thinnest LDL values along the axis floor.

From these observations and the smooth, nearly symmetrical ridge morphology, we interpret the RW1 ridge to be a narrow exhumed ridge bounded to the east by an east-facing detachment fault. We interpret the change in slope, prominent in the center of the segment, to be the termination of the detachment fault (red thin line with ticks and red and blue dashed line in Figures 2b, 3, 4a, and 6). The thin LDL extending from the center of RW1 to the valley floor supports the absence of magmatic crust on this side of the ridge axis, and therefore the interpretation as a detachment fault. The ridge crest delimits the breakaway of this fault (BW1, ~25°34′W). The fault scarp appears to have been eroded, as shown by the numerous gullies. Only a few other normal faults were mapped on this side of the axial valley.

4.2. Off Axis Morphology and Structure: the Western Ridge Flank

The morphology of the western flank of the segment is dominated by smooth surfaces separated by heavily faulted lows and areas with rugged topography (Figures 1 and 2). Between 26°20′W and the present-day ridge axis, the morphology alternates large and smooth bathymetric highs and narrow lows extending over the whole length of the segment (Figures 2, 4, and 6). Moving west from RW1, a couple of ridges are observed (named RW2 and W1). We identify two structures, named W2 and W3, displaying smooth morphology and spreading-parallel corrugations, which we interpret to be fragments of detachment surfaces.

The ridge RW2 has steeper flanks and is narrower than RW1, except for a domed eastern flank in the north. It is oriented N160°E, that is, slightly oblique to the orientation of the axis, and displays a smooth western flank and an irregular eastern flank affected by faults oriented N40–45°E. It reaches the depth of ~3,000 m and is separated from RW1 by a narrow basin (Figures 2, 4a, and 6). Between the two ridges, a smooth undetermined area surrounds some conical seamounts and hummocky terrains that form one of the rare prominent volcanic terrains observed off-axis in the whole study area. The LDL thickness is asymmetric, with low values (4.5 km) to the north and slightly higher values (6 km) to the south. We interpret the ridge RW2 to consist of exhumed, mantle-derived rocks. It is difficult to delimit with certainty the detachment fault bounding the structure. However, the significant changes in the morphology of this ridge can be used to delimit its breakaway and termination. The ridge crest is identified as the breakaway (BW2, ~25°40′W) of this small detachment and the break of slope to the east of this structure is inferred to be its termination (Figures 2b, 4, and 6).

Between 25°44′W and 25°49′W, we observe two elongated ridges parallel to RW1 and RW2, merging to the south into a single ridge, altogether forming a complex feature, which we called W1 (Figures 2, 4b, and 6). The two ridges, separated by a roughly oval-shaped basin, display similar characteristics. Their flanks are formed by smooth surfaces without traces of corrugations or volcanic morphology. A dredge haul on the south-western part of the western ridge (COL-DR30) contained several blocks of gabbroic rocks (Figure 3a). Gabbro mylonites reveal that the rocks underwent strong ductile deformation starting close to magmatic conditions. Rocks derived from a basaltic dike were also collected in the dredge. The gravity inversion shows that the ridge is located in an area of thin LDL (3.5–4.6 km) (Figure 3b). We interpret the whole W1 feature to represent a heavily faulted detachment surface, and the crest of the westernmost ridge to be its breakaway (BW3, ∼25°49′W). This detachment surface does not show a termination, but is bounded to the east by a large high-angle normal fault scarp. The W1 feature is separated from RW2 by a large basin with rough morphology and smooth and homogeneous reflectivity associated with low values of the LDL thickness (3.2–4.7 km), which could consist of highly fractured and dismantled altered mantle, possibly coated with a thin layer of volcanics and sediments.

West of W1, we observe two fragments of smooth surfaces displaying low reflectivity and traces of corrugations, which we interpret as parts of long-lived detachment surfaces. These two corrugated surfaces, about 26 and 28 km-wide respectively, extend from 25°50′W to 26°03′W (W2), and from 26°06′W to 26°20′W (W3) (Figures 2, 4, and 6). Like W1, the structures do not present the entire morphology of typical oceanic core complexes. The corrugated surfaces are dissected by normal faults and do not display clear terminations but east-facing high-angle normal fault scarps instead. As for the previously described RW1 to W1 structures, these OCC fragments are bounded to the west by smooth and very narrow basins, parallel to the spreading axis and about 500 m deeper than the surrounding topography (Figures 2, 4, and 6). These probably partly result from the rotation of the detachment faults during their development.

The smooth W2 detachment surface shows few discontinuous corrugations in its northern part, 50–100 m in amplitude, spaced by 1–1.5 km (Figures 2, 4c, 4d, and 6). The breakaway (BW4, near 26°03′W) is a relatively sharp ridge roughly parallel to the present-day ridge axis and is characterized by a smooth morphology, without clear volcanic features. The west-facing slope of this breakaway dips about 20°, and its southern part has been disrupted by mass wasting. Several ridge-parallel, east-dipping normal faults cut the corrugated surface, creating a topography of small horsts and grabens. The samples retrieved at the eastern side of W2 (COL-DR31) are very similar to those of dredge COL-DR30, that is, variably deformed gabbroic rocks (Figure 3a). Over the entire southern part of this detachment surface, highly affected by landslides and mass-wasting, the LDL thickness is ∼2 km (Figure 3b). The northern smooth and partly corrugated part presents a thicker LDL (from 4.3 to 4.5 km).

The second corrugated surface, W3, is very flat, smooth and displays the most prominent corrugations of the study area (Figures 2, 4d, 4e, and 6). As W2, the western end of this structure is marked by a sharp ridge (∼26°20′W), which has a west-facing slope dipping about 20°, displaying secondary, west-dipping faults (Figures 2 and 6), and which could correspond to its breakaway (BW5). As for the breakaway of W2, we do not observe clear volcanic morphologies and this ridge is characterized by smooth surfaces on both sides. The northern and southern flanks of this structure are largely affected by erosion and mass wasting, which probably highly reduced the area of the original smooth and corrugated surface (Figure 4e). The gravity-derived LDL shows slightly higher thickness values (∼6.6 km) in the central part of the structure. To both west and east, the LDL thickness decreases to ∼3 km near the breakaway ridge and 5.4 km near a normal fault bounding the structure to the east. Although we have no direct evidence for the nature of the rocks, the thickness of the LDL and the presence of clear corrugations suggest that the W3 structure is part of a typical OCC including gabbros and probably some serpentinized peridotite, which can lead to overestimate the LDL thickness along W3.

4.3. Off Axis Morphology and Structure: The Eastern Ridge Flank

East of RE1, we observe a small area of volcanic seafloor ∼3 km wide characterized by high and heterogeneous reflectivity (Figure 5b). To its east, an area ∼10-km-wide displays smooth terrain with gentle topographic relief, no clear volcanic structure or faulting pattern, slightly heterogeneous acoustic backscatter, and no evidence for a detachment surface or abyssal hills (Figures 2c and 5a). The LDL here is ∼5.5 km thick (Figure 3b). We posit that this area, named "smooth undetermined area," is mainly composed of deep crustal or mantle rocks with a very thin basaltic cover producing a smooth and relatively flat morphology.

Further east, three prominent ridges, which we have labeled E1, E2, and E3 from west to east, show a half-dome asymmetric morphology. Their western flank is marked by a steep, west-facing scarp sub-parallel to the axis, sometimes associated with a rather smooth and faulted bulge. Their convex eastern flank is marked by smooth surfaces typical of OCC surfaces and terminations. The east-facing detachment surfaces of E2 and E3 also show prominent corrugations (Figures 2, 5, and 6). From west to east, these three structures are ∼21, 14, and 12 km long, respectively, and their summits reach depths of ∼2,500 m. They are separated by saddles or basins ∼6 km wide reaching depths between 3,700 and 4,000 m (Figures 2, 5, and 6).

The first off-axis ridge on the east flank, E1, near 25°12′W (Figures 2, 5b, and 6), extends to almost the entire segment length. It is shallower and wider in its southern part. It shows a steep west-facing flank, with a rough morphology marked by normal faults and massive landslides (Figures 2 and 5b). The eastern side of the ridge, convex to the east, has a smooth morphology with a high and homogeneous reflectivity area that suggests recent mass wasting. We associate a change in slope and reflectivity at its base with the termination of an east-facing detachment. The ridge E1 is associated with a 4.9–5.9 km-thick-LDL (Figure 3b). Dredge COL-DR28, on the western scarp of the ridge, near its central part, returned a large block of olivine gabbro (Figure 3a). East of the E1 ridge, the bathymetry shows a 3,600 m-deep low displaying a smooth seafloor, which also extends over the entire length of the segment (Figures 2, 5b, and 6). The LDL thickness here is about 5.5 km on average (Figure 3b). This basin is interpreted to have been the axial valley when the detachment fault was active, forming E1, now abandoned.

Near 25°06′W, the ridge E2 displays a half-dome morphology and a topographic profile similar to E1, with a steep western flank and a smooth eastern flank (Figures 2, 5c, and 6). The convex eastern ridge side is smoother than that of the E1 ridge and shows well-marked corrugations. The LDL is relatively thin on the northern part of the ridge (∼4.6 km), where the dredge COL-DR27 was realized, and slightly thicker (5.3 km) on its southern part (Figure 3). On the western flank of the E2 ridge, dredge COL-DR27 sampled rocks with variably deformed crustal lithologies (Figure 3a), including mylonitic serpentinites, which document a shear zone active from high T (>800°C, de Brito, 2019) to sub-seafloor conditions. A gabbroic mylonite sample contains boudins of a microcrystalline gabbroic ultramylonite (see sample picture in Figure S3 in Supporting Information S1), suggesting multiple shearing events in a fluctuating thermal field. We interpret this side of E2 ridge as a section across the shear zone beneath the exhumation surface while the base of E2 eastern flank corresponds to the termination of the detachment fault. The ridge E2 is also bounded by a bulge at the base of its western flank, mostly due to erosion and mass wasting. The bounding bulge presents the same LDL signature as the ridge, suggesting that it is composed mainly of lower crust or serpentinized peridotites. Moreover, as for the basin east of E1, we interpret the elongated basin just east of E2 and associated with a ∼6 km-thick LDL to be the ancient axial valley coeval to the activity of the E2 detachment.

We observe a third ridge, E3, near 24°53′W (Figures 2, 5d, and 6). Ridge E3 displays the same morphology as the E2 ridge: a convex, half-dome eastern flank with smooth morphology and corrugations, and a rougher and steeper western flank associated with a bulge. Eastward, the ridge is surrounded by flat and deep basins. The half-dome ridge as well as the associated bulge correspond to an area of thin LDL, among the lowest values estimated in this area (∼2.7 km) (Figure 3b). Eastward, the basin is underlain by a variably thick LDL (3.2 km in the south to 6.7 km in the north). Dredge COL-DR26, on the southern part of the ridge eastern slope, recovered a high diversity of rocks: basalt, gabbro, serpentinites and mylonites showing variable degrees of deformation and weathering (Figure 3a). As for E2, we interpret the ridge E3 to represent the terminal part of a detachment surface and the eastern basin, an ancient axial valley coeval with the detachment. The very round bulge on the western side of the structure is larger than the ones observed for E1 or E2, and larger than an expected talus. The very thin LDL (∼2.5 km) suggests that it could consist of deep crustal or mantle rocks from the core of the OCC dome, after the erosion of the detachment surface.

The easternmost bathymetric high in the study area forms a nearly circular structure from 24°46′W to 24°30′W, bounded by a NW-SE-trending ridge on the east and a smaller ridge oriented N160°E. This oblique feature, covered in part by sediments, was not sampled by dredging.

5. Discussion

Our observations reveal an overall magma-poor spreading at the southern intra-transform ridge segment of the St. Paul system, dominated by detachment faults and exhumation of lower crustal and mantle rocks. The structural patterns are very asymmetric with respect to the ridge axis, and they appear to vary with time within our survey

area. We discuss a scenario for the generation and evolution of the structures from old to young seafloor, their frequent obliquity, and the implications for the magma budget of this short intra-transform segment.

Because of the strong asymmetry of the structures between either ridge flanks, the proximity to the magnetic equator and the delayed magnetization of the peridotite during its serpentinization (Sichler & Hékinian, 2002), strict temporal constraints cannot be easily inferred. An age of ∼6 Myr can be estimated for the seafloor near 26°20′W on the western ridge flank, by assuming a constant and symmetric full spreading rate of 32 mm/y (DeMets et al., 2010). The matching structures on the eastern flank extend to about 24°45′W, or about 5 Ma with a similar age estimate. As explained in the following sections, we believe that within these boundaries, the structures on either side of the axis are conjugate and we suggest a scenario for the development of the segment since that time. The overall study area for this segment extends to about 10 Ma on the western flank.

5.1. Reconciling the East and West Flanks: Evolution of the Ridge Segment From About 6 to 1.5 Ma Through Oceanic Core Complex Development and Splitting

We showed in Section 4 how most of the observed ancient features on each ridge flank could be interpreted as partially dismembered areas of detachment faults or OCCs. The distribution of these features appears to be strongly asymmetric on the two flanks of the ridge. Breakaways and smooth corrugated surfaces are observed on the west flank, bounded to their east by large east-facing scarps (Figures 4c, 4d, 4e, and 6) while "half-dome" terminations are identified on the east flank, bounded to their west by west-facing scarps and associated to some irregular terrains (Figures 5b, 5c, 5d, and 6). We interpret this asymmetric distribution as resulting from the repeated splitting of the young part of east-dipping low-angle detachment faults related to three OCCs (Figures 7 and 8). Assuming that the detachment surfaces observed on either flank once formed continuous OCCs, we tentatively match the conjugate components to reconstruct the former OCCs (Figure 7).

The oldest corrugated surface W3 (west flank) and the E3 half-dome (east flank) once formed a single OCC (OCC3, Phase 1, Figure 7). Similarly, the W2 corrugated surface (west) has its corresponding termination E2 on the east flank, and both structures formed OCC2 in the past (Figure 7). The W2 detachment surface appears partially rifted, forming several horsts, implying that OCC2 was affected by extension before being split by a new detachment fault. Axis-parallel scarps bounding E3 and E2 to the west mark the location of the main ruptures and the limits of the transferred lithospheric blocks; we named these scarps "splitting scarps" (Figures 2c, 5c, 5d, and 6). East of E2, there is no evidence for well-developed volcanic abyssal hills that would have been coeval to the development of OCC2. This observation suggests that the magma supply remained relatively low during its development, and that the accretion was highly asymmetric, with mostly gabbro emplacement at depth in the footwall and very low volcanism.

On younger seafloor, the observed morphologies suggest that W1 and E1 once formed OCC1, generated during Phase 5 then faulted and split during Phase 6 (Figure 7). The tectonic origin of these structures is supported by sampling of variably deformed gabbros on both E1 and W1, suggesting tectonic exhumation as the main crust-building process. The absence of corrugation on this OCC might reflect a lower melt supply compared to typical OCCs, with a lower rheological contrast between footwall and hanging wall preventing the formation of corrugations (Spencer, 1999; Spencer & Ohara, 2008, 2014; Tucholke et al., 2008). Alternatively, the formation of corrugation might be due to a "brittle factory" located at a depth of ∼4 km along the detachment fault (Parnell-Turner et al., 2018), so that the juvenile portion of a detachment does not show any corrugations. This OCC-type feature may correspond to a short-lived detachment fault, now highly eroded and disrupted by normal faults.

The rifting of an OCC has been described by Reston et al. (2002) and Planert et al. (2010) along the MAR near 5°S, where two corrugated massifs on either side of the ridge axis show morphologies very similar to those described here (OCC1, OCC2, and OCC3). Based on seismic tomography data analysis, Planert et al. (2010) suggested that the rifting of the 5°S MAR OCC was associated with a very low melt supply. Different mechanisms have been suggested to stop the development of detachment faults, such as the associated bending stresses becoming too large (Buck et al., 2005; Lavier et al., 2000), or a sudden increase of the magma input (MacLeod et al., 2009), or more precisely, increased magma input in the brittle layer (Olive et al., 2010). In the former case, a new fault forms in the hanging wall or in the footwall of the original detachment, usually, but not necessarily, with an opposite sense, in a "flip flop" dynamic (Lagabrielle et al., 1998; Reston, 2018; Sauter et al., 2013). In the second case, the spreading becomes accommodated by diking and formation of ridge-parallel volcanic abyssal hills.

In our case study, we do not observe significant volcanic constructions between the detachment surfaces, while the development of extensional faulting within the OCC (e.g., W2, Figures 4c and 4d) suggests a decreased

10.1029/2023GC010870

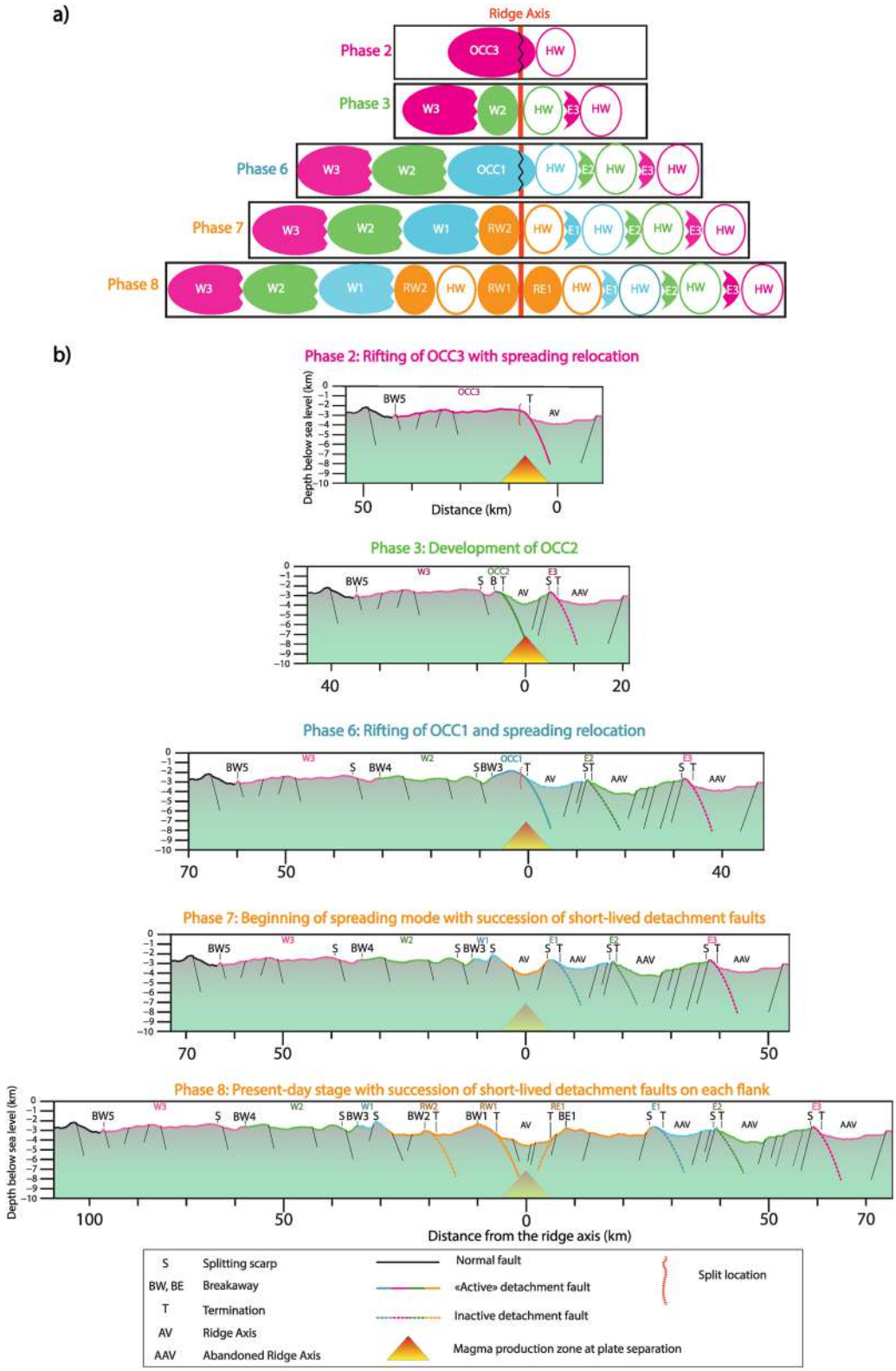

Figure 7.

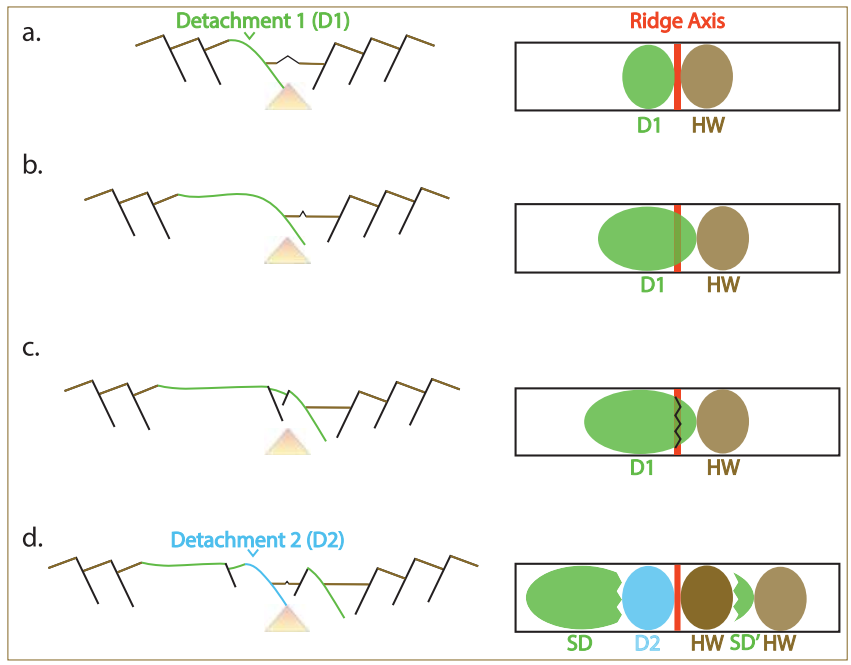

Figure 8. Schematic cartoon illustrating the development and termination of the OCCs observed along part of ITRS 3 since 6 Ma. The left part of the cartoon corresponds to a cross section view and the right part corresponds to a view from the top. (a) Initial stage showing the birth of the OCC and growth of the detachment fault. The magma supply is relatively low but enough to ensure the emplacement of gabbros at the OCC core. The value of *M* (ratio of magma input to tectonic deformation accommodating the ridge spreading) is likely between 0.5 and 0.3 (Tucholke et al., 2008). (b) Growth of the OCC as the melt supply at the ridge axis decreases. During this time, the plate boundary (termination) tends to migrate toward the hangingwall because no magmatic accretion occurs on the eastern side of the axis. (c) The excessive eastward migration of the footwall brings the OCC dome to override the region of heat focusing over the area of magma production zone at plate separation. Bending stress and heat excess in the footwall leads to the formation of one or several new normal faults and the relocation of the ridge axis in the footwall. (d) The OCC is rifted and the block comprising the termination, accompanied by the abandoned axial valley, is drafted away on the eastern flank of the ridge. Since there is no increase in the magmatic input compared to the initial stage, a new OCC is formed during the creation of a new axial valley. The breakaway of this new detachment is forming in the previous detachment, thus explaining the absence of volcanic hummocky terrains on the outer flank of the breakaways. The abbreviations correspond to: Hanging Wall (HW); Split Detachment (SD and SD'). As in Figure 7, the orange triangle represents the area of magma production zone at plate separation. The top view is based on a figure from Hayman et al. (2011) and the cross-section view is based on a figure from Macleod et al. (2009).

magma supply during inter-OCC phases. The observation of peridotites or highly deformed deep crustal rocks near the termination of the detachment faults in the half-dome ridges suggests that the abandonment of these faults may coincide with periods of low magma input, with fewer gabbros emplaced at depth. From numerical models, Tucholke et al. (2008) or Olive et al. (2010) showed that a detachment fault can lock in a context of low *M* ratio. They show that when the *M* ratio reaches values below 0.5, the detachment fault termination (plate boundary) tends to progressively migrate toward the hanging wall, producing an asymmetry in the spreading and in the thermal structure of the ridge axis. Heat advection to the footwall, associated with the increase in the bending stresses, leads to the break-off of the footwall. In these authors' models, a new master fault takes over plate separation and creates a new detachment surface. This same model shows that if the *M* ratio reaches values as low

Figure 7. Kinematic model for the St. Paul ITRS 3 from (a) a top view and (b) a cross section view where the different stages of spreading are identified by colored solid lines. Thicker solid lines indicate active detachments. Dashed solid lines represent the inactive detachment faults. The cartoon of the latest phase (phase 8) is produced from the current bathymetry. The vertical exaggeration is X2. The different phases represented were chosen to show the most important steps of the segment evolution. See Section 5 for details. The orange triangle represents the area of magma production zone at plate separation. The lighter and darker triangles represent the reduction of melt supply at the ridge axis (see part 5.1 and Figure 8 for more details). Phases 1, 3, and 5 correspond to the phases of the generation of OCC3, OCC2, and OCC1. Phases 2, 4, and 6 correspond to the rifting of these structures ending in westward spreading axis relocation. Phase 7 shows the beginning of the successive formation of short-lived detachments with no evidence of splitting. Phase 8 corresponds to the present-day spreading mode with the presence of short-lived detachment faults on each flank of the ridge. Because they are identical to phases 2 and 3, phase 1 (development of OCC3), phase 4 (rifting of OCC2 and spreading relocation) and phase 5 (development of OCC1) are not represented in order to facilitate the reading of the figure.

as 0.3, the detachment fault termination will migrate faster in the direction of the hanging-wall associated with an increasing number of high-angle normal faults intersecting both the hanging wall and the footwall.

We infer that the evolution of OCCs 1–3 in our survey area can be described by such a mechanism, summarized in Figure 8. The low magma supply ($0.5 < M < 0.3$) leads to the migration of the detachment in the direction of the hanging wall, bypassing the area of plate separation in the mantle (Figure 8b). The decrease in magma supply at the base of the detachment fault stops the motion along the main fault, leading to extension within the footwall (Figure 8c). This internal extension is focused on the line of maximum heat advection, that is, the area of magma production zone at plate separation (orange triangle in Figures 7 and 8), generating the rupture of the footwall along one or several high-angle normal faults (Figures 8c and 8d). The axis relocation splits the OCC, leaving the faulted corrugated surface with the breakaway on the west flank, and the abandoned axial valley with the half-dome termination morphology on the east flank (Figure 8d). Part of the old detachment, west of the new axis, is re-mobilized near the breakaway by the new detachment. This scenario explains the absence of a volcanic hummocky morphology on the outer flank of the breakaway.

In this scenario, the asymmetry implied by the motion on large-offset detachment faults is partly compensated by the westward plate boundary relocation on new detachment faults, which transfers portions of the western flank lithosphere to the eastern flank. Considering the ∼20–30 km widths of the present-day axial valley and of the detachment fragments on the east flank, and given the 30 km/Myr full spreading rate, we estimate that these processes take place in the axial domain, every ∼1.5–1 Myr. The mechanism sketched in Figure 8 appears to have repeatedly acted, leading to the splitting of W3-E3, W2-E2, and W1-E1 systems, so that this mechanism is probably generic of OCC termination in the context of low melt supply, as suggested by Planert et al. (2010). The presence of rifted OCCs is therefore likely observable along other ridge sections presenting these particular conditions.

5.2. Recent Spreading Phase: Formation of Short-Lived Detachment Faults

Both axial valley walls are formed by uncorrugated and short-lived detachment faults (RW1 and RE1, horizontal offset of ∼5.7 and ∼3.6 km respectively). The flipping polarity of successive detachment faults marking the plate boundary is usually proposed to explain two detachments facing each other (e.g., Cannat et al., 2006; Escartin et al., 2008; Reston, 2018; Sauter et al., 2013; Schroeder et al., 2007; Tucholke et al., 2008). Due to their proximity with the ridge axis, one of the detachment faults that formed RW1 or RE1 is likely to be still active but both surfaces are affected by erosion and mass wasting, so that it is not possible to identify an active fault without any seismic study of the area. Because the detachment surface of RW1 observed on the west flank is smoother, less affected by landslides and normal faults (Hekinian et al., 2000) than that of RE1, we interpret the ridge RW1 as the most recent detachment structure. Moreover, the RW1 detachment fault shows the thinnest portion of LDL at the ridge axis (Figure 3b), consistent with low magmatism and thin lithosphere associated with a recent fault (Behn & Ito, 2008; Escartin et al., 2008).

The volcanic structures on the bottom and to the east of the axial valley (Figures 2, 4a, and 5a) are also recent to present-day features, and likely coeval to the detachment in the west (RW1), altogether representing the most recent spreading phase (Figure 7, Phase 8). The western flank of the ridge RW1 (west of BW1; Figures 2, 4a, and 4b) presents a small volcanic area with seamounts and appears to be the coeval western portion of the detachment fault that formed RE1. We note that both the breakaways of RE1 and RW1 have volcanic surfaces, indicating that they have been uplifted from a volcanic seafloor with a very thin basaltic layer, such as what was observed by Hekinian et al. (2000) in the near-axis area.

Farther away from the axis on the western flank, we interpret RW2 to be a ridge resulting from a previous short period of mantle-derived rock exhumation. The absence of clear corrugated surfaces or hummocky terrains suggests limited magma emplacement during the exhumation of RW2. The coeval portion to the east is possibly represented by the flat and smooth area between RE1 and E1 and interpreted to consist of lower crustal and mantle rocks covered by a thin basaltic shell. These features, derived from mantle exhumation and sparse volcanism, are also included in Phase 8 (Figure 7).

The recent spreading phase therefore appears to be dominated by detachment faults that have been active over shorter periods of time (offset less than 6 km) compared to the previous spreading phases presented in this study. Moreover, the recent short-lived detachment faults (RE1, RW1, and RW2) present complete detachment structures with no evidence for splitting. We propose that the chronological order of formation of the structures was

RW2, then RE1, and finally RW1, so that the polarity of the detachment faults has flipped from one flank to the other, producing a symmetrical accretion over time (Figure 7).

The structures described for the recent segment evolution show some similarity with the "smooth seafloor" described in areas of amagmatic mantle exhumation along the eastern Southwest Indian Ridge (SWIR; Cannat et al., 2006; Sauter et al., 2013). The smooth ridges RW2, RW1, and RE1 appear to consist largely of peridotite and display a nearly symmetrical morphology. However, the smooth ridges observed along the SWIR present exhumed peridotite surfaces on both flanks due to their emergence from an earlier detachment fault surface, whereas a thin cover of basalt is observed on some of the breakaways and in the axial valley in our study area. This observation suggests that the detachment faults are coeval with some volcanic activity but producing only a very thin volcanic layer (Hekinian et al., 2000; Sichler & Hékinian, 2002).

5.3. Tectonic Styles, Obliquity, and Asymmetry

The axial valley presents two detachment faults facing each other. The flipping polarity of detachment faults is generally observed in amagmatic or nearly amagmatic contexts (Lagabrielle et al., 1998; Reston, 2018; Sauter et al., 2013). However, the early detachments in our study area formed consecutively on a single flank of the ITRS 3, which suggests that the deformation was controlled by factors other than peridotite deformation. We suggest that the various deformation styles observed along the ITRS 3 might reflect the differences in mechanical coupling along the transform faults on either end of the spreading segment. In the recent times, the serpentinization of the mantle exhumed on detachment faults likely favors decoupling along the transform faults, thus minimizing the role of the transform fault shear stresses. These variations in the role of the transform fault shear stresses might also explain the variations in the time of the obliquity of the structures with respect to spreading.

The systematic development of new east-facing detachments on the western side of the axis might be related to the difference in offsets of the transform faults bounding the ridge segment, 87 and 33 km for the north and south boundaries, respectively. Buck et al. (2005) proposed that large-offset normal faults might be preferentially located on the inside corner side of the axis because this setting minimizes the shear strain across the transform fault. In the case of our intra-transform ridge segment, it is possible that the larger offset of the northern transform fault compared to the southern one, implying larger shear strain, favors a setting where east-facing detachment faults on the western flank are favored.

5.4. Implications of the Observed Structures for the Magma Budget of ITRS 3

The major tectonic pattern described here consists of the repeated split of consecutive OCCs, and the reverse polarity of short-lived detachment faults (Figures 2, 6, 7, and 8) during a period fully dominated by detachment-type extension. The seafloor morphology and the gravity-inferred thin LDL on the western ridge flank beyond our study area (Figures 2a and 3) suggest that another long-lived OCC formed before 6 Ma. Hence, detachment-dominated spreading has possibly characterized the accretionary processes of the ITRS 3 over the last 10 Myr.

The development of oceanic core complexes and "smooth seafloor" ridges as described in the last decades has been associated to relatively low magma budgets ($M \leq 0.5$) (e.g., Cann et al., 1997; Cannat et al., 2006; Ildefonse et al., 2007; MacLeod et al., 2009; Okino et al., 2004; Sauter et al., 2013; Smith et al., 2006; Tucholke et al., 1998), and associated more specifically to low magma injection rate in the brittle lithospheric layer (Olive et al., 2010). Accordingly, the M ratio between magma emplacement and tectonic stretching in our study area is estimated to range from 0.3 to 0.5, accompanied by significant strain weakening along the large-offset normal fault, and reduced thickening of the lithosphere away from the axis (Buck et al., 2005; Lavier et al., 1999; Tucholke et al., 2008).

The gabbro samples collected on the detachment surfaces on the western ridge flank show that the segment received some magma and supports the hypothesis that OCCs have a gabbroic core (Ildefonse et al., 2007) derived from melt injections in the footwall (MacLeod et al., 2009; Manatschal et al., 2011). However, the total budget is reduced enough to never allow the formation of a continuous basaltic layer, as suggested by the limited amount of volcanic terrains mapped here.

Some observations are supportive of a decrease in melt supply from OCC3 to OCC2. First, the detachment surface W3 is not faulted as the surface W2, indicating that the relocation of the spreading axis was entirely

focused in the splitting region, probably implying a shorter phase of low magma input compared to the dismantlement of W2. Second, the OCC3 is larger, implying that the detachment has been active over a longer time. Third, the presence of more marked corrugations suggests the presence during the exhumation of a more brittle (more basaltic and gabbroic) hanging wall over a more ductile footwall (Spencer, 1999). Finally, the LDL thickness values along W3 are slightly higher than for the W2 structure (Figure 3b), implying a thicker crust and therefore a greater magma supply.

During the recent spreading phase, some sparse volcanic seafloor areas are observed between the exhumed surfaces RW1 and RW2 and east of the RE1, forming the breakaway of this exhumed ridge (Figures 2b, 4a, 4b, and 5a). These volcanic areas could represent possible short-time increases in the melt supply. Significant increases of magma supply to the ridge axis would terminate the motion on the detachment, but it would imply the creation of thicker basaltic crust and the formation of abyssal hills bounded by high-angle normal faults. Such volcanic spreading structures are not observed on ITRS 3 flanks. It is therefore more likely that the recent phase has a low magmatic supply, even lower than the earlier spreading phases.

The change from OCCs to smooth ridges suggests that the overall low magma budget decreases from ∼6 to ∼1.5 Ma. It is here interpreted as reflecting an evolution from a spreading mode with the formation of gabbro-cored OCCs with short periods of volcanic activity to short-lived detachments exhuming mainly mantle rocks. This later spreading mode is close to smooth seafloor-type structures found along the SWIR but does not reach the characteristic amagmatic state (Cannat et al., 2006; Sauter et al., 2013). The intermediate structure is represented by OCC1, which we interpret to include less gabbros, and which developed during a lower magma input period than typical OCCs, preventing the formation of a long-lived detachment surface and the associated corrugations.

The change in structure and morphology over time is likely controlled by the *M* ratio. As previously discussed, OCCs form for *M* ratios between 0.3 and 0.5, whereas mantle exhumation and "smooth seafloor" tectonics occur where *M* is lower than 0.3 (Olive et al., 2010; Tucholke et al., 2008). A lower *M* ratio (<0.3) results in a more systematic and faster migration of the detachment termination toward the hanging wall, likely shortening the lives of the detachment faults (Tucholke et al., 2008). The recent part of the ITRS 3 with multiple smaller detachment faults exhuming peridotite on each flank of the axial valley could therefore reflect a low *M* ratio, lower than the older parts showing long-lived detachment faults.

A decrease in spreading rate during the last ∼6–7 Myr suggested by kinematic models of the South Atlantic (e.g., DeMets & Merkouriev, 2019) could account for the decrease in melt production. Another explanation could be a decrease in the temperature (Schilling et al., 1995) or fertility of the sublithospheric mantle. Yet another hypothesis is the increase in axial lithosphere thickness due to enhanced hydrothermal cooling that is induced by the continuous formation of large-offset faults (Escartin et al., 2008; Olive & Dublanchet, 2020). These hypotheses are very likely to be complementary. If an anomalously cold rising mantle reduces the magmatic supply at the surface it may initiate the development of detachment fault. The detachment fault will then increase deep cooling, further reducing the magmatic input, the *M* ratio and generating a different mode of spreading. Unfortunately, the current data do not allow us to infer the cause of the possible reduction of *M* with time and further study along the ITRS 3 would be necessary for this.

6. Conclusions

The tectonic, geophysical and petrographic analysis of the St. Paul ITRS 3 reveals that, over the last ∼6 Myr at least, the segment has been dominated by the development of detachment faults. The ridge flanks morphology shows a progressive change in the segment structure with the presence of fragments of smooth, corrugated surfaces in the older part and smaller surfaces exempt of corrugations, and sparse volcanic seafloor in the youngest part. The rocks dredged on these reliefs mostly include gabbros, peridotites and serpentinites. We propose a model of evolution of the segment with a progressive change in the mode of accretion. We suggest that the decrease of melt supply over time is the main factor controlling this change. The accretionary processes evolved from the development of corrugated OCCs on one ridge flank only to the formation of short-lived detachment faults on both flanks, with a transition period that formed a shorter OCC free of corrugations. The older phases show the development of large detachment faults forming OCCs, which were split by westward spreading axis relocation, leaving parts of each OCC on either ridge flanks. The spreading relocation tends to restore a part of the symmetry of spreading following asymmetric spreading along OCCs. As suggested by the recurrence of rifted

detachments along part of ITRS 3 since ~6 Myr, the rifting and splitting of OCC seems to be a generic mechanism related to the termination of detachments and is certainly observable along other portions of mid-ocean ridges in a context of very low magmatic input.

Data Availability Statement

The gridded geophysical shipboard data set on the South Intra-Transform segment of the St. Paul transform system (COLMEIA cruise) supporting the conclusions presented in this manuscript is available via the SEANOA archive website (at https://doi.org/10.17882/92690; Maia et al., 2023).

Acknowledgments
COLMEIA cruise ship time (Maia, 2013, https://doi.org/10.17600/13010010) was granted by the TGIR French Oceanographic Fleet. This work was supported by grants from CNRS-INSU "Campagnes à la mer", CNRS-INSU-Syster, Labex MER and Région Bretagne, France, and from Universidade Federal Fluminense and CPRM, Brazil. D.B. was funded by the Italian Programma di Rilevante Interesse Nazionale PRIN2017KY5ZX8. M.L. acknowledges supporting grant PRIN 20125JKANY_002 from the Italian Programma di Rilevante Interesse Nazionale. C.V. received support from the Korea Institute of Energy Technology Evaluation and Planning (KETEP) and the Ministry of Trade, Industry & Energy (MOTIE) of the Republic of Korea (No. 20168510030830) as well as the National Research Foundation of Korea (NRF) grant funded by the Ministry of Science Information and Technology (MSIT), Korea (Fund No. 2022R1A5A1085103). Thanks is provided to SECIRM, Brazilian Navy, for their help and support to this project. We are grateful to Captain G. Ferrand and his crew from R/V L'Atalante, to the technical staff of GENAVIR, and to the COLMEIA science party for their help on acquiring and processing the data presented here. We also thank Professor Jeff Karson and two anonymous reviewers for their constructive reviews that led to significant improvements in the manuscript. Our seismic data set was completed using lines from the NCEI Marine Trackline Geophysical Data bank (https://www.ncei.noaa.gov/products/marine-trackline-geophysical-data). Publication fees funded by Université de Bretagne Occidentale through the COUPERIN consortium.

References

Anderson, E. M. (1951). The dynamics of faulting, Etc. (Revised.).
Behn, M. D., & Ito, G. (2008). Magmatic and tectonic extension at mid-ocean ridges: 1. Controls on fault characteristics. *Geochemistry, Geophysics, Geosystems*, *9*(8), 8–10. https://doi.org/10.1029/2008GC001965
Blackman, D. K., Canales, J. P., & Harding, A. (2009). Geophysical signatures of oceanic core complexes. *Geophysical Journal International*, *178*(2), 593–613. https://doi.org/10.1111/j.1365-246X.2009.04184.x
Blackman, D. K., Cann, J. R., Janssen, B., & Smith, D. K. (1998). Origin of extensional core complexes: Evidence from the Mid-Atlantic Ridge at Atlantis fracture zone. *Journal of Geophysical Research*, *103*(9), 21315–21333. https://doi.org/10.1029/98jb01756
Blackman, D. K., Ildefonse, B., John, B. E., Ohara, Y., Miller, D. J., Abe, N., et al. (2011). Drilling constraints on lithospheric accretion and evolution at Atlantis Massif, Mid-Atlantic Ridge 30N. *Journal of Geophysical Research*, *116*(B7), B07103. https://doi.org/10.1029/2010jb007931
Bonatti, E. (1990). Subcontinental mantle exposed in the Atlantic Ocean on St. Peter-Paul islets. *Nature*, *345*(6278), 800–802. https://doi.org/10.1038/345800a0
Bonatti, E., Brunelli, D., Fabretti, P., Ligi, M., Portaro, R. A., & Seyler, M. (2001). Steady-state creation of crust-free lithosphere at cold spots in mid-ocean ridges. *Geology*, *29*(11), 979–982. https://doi.org/10.1130/0091-7613(2001)029<0979:SSCOCF>2.0.CO;2
Bonatti, E., Seyler, M., & Sushevskaya, N. (1993). A cold suboceanic mantle belt at the Earth's equator. *Science*, *261*(5119), 315–320. https://doi.org/10.1126/science.261.5119.315
Brunelli, D., Sanfilippo, A., Bonatti, E., Skolotnev, S., Escartin, J., Ligi, M., et al. (2020). Origin of oceanic ferrodiorites by injection of nelsonitic melts in gabbros at the Vema Lithospheric Section, Mid Atlantic Ridge. *Lithos*, *368–369*, 105589. https://doi.org/10.1016/j.lithos.2020.105589
Brunelli, D., & Seyler, M. (2010). Asthenospheric percolation of alkaline melts beneath the St. Paul region (Central Atlantic Ocean). *Earth and Planetary Science Letters*, *289*(3–4), 393–405. https://doi.org/10.1016/j.epsl.2009.11.028
Buck, W. R., Lavier, L. L., & Poliakov, A. N. B. (2005). Modes of faulting at mid-ocean ridges. *Nature*, *434*(7034), 719–723. https://doi.org/10.1038/nature03358
Cann, J. R., Blackman, D. K., Smith, D. K., McAllister, E., Janssen, B., Mello, S., et al. (1997). Corrugated slip surfaces formed at ridge-transform intersections on the Mid-Atlantic Ridge. *Nature*, *385*(6614), 329–332. https://doi.org/10.1038/385329a0
Cannat, M., Mangeney, A., Ondréas, H., Fouquet, Y., & Normand, A. (2013). High-resolution bathymetry reveals contrasting landslide activity shaping the walls of the Mid-Atlantic Ridge axial valley. *Geochemistry, Geophysics, Geosystems*, *14*(4), 996–1011. https://doi.org/10.1002/ggge.20056
Cannat, M., Sauter, D., Escartín, J., Lavier, L., & Picazo, S. (2009). Oceanic corrugated surfaces and the strength of the axial lithosphere at slow spreading ridges. *Earth and Planetary Science Letters*, *288*(1–2), 174–183. https://doi.org/10.1016/j.epsl.2009.09.020
Cannat, M., Sauter, D., Lavier, L., Bickert, M., Momoh, E., & Leroy, S. (2019). On spreading modes and magma supply at slow and ultraslow mid-ocean ridges. *Earth and Planetary Science Letters*, *519*, 223–233. https://doi.org/10.1016/j.epsl.2019.05.012
Cannat, M., Sauter, D., Mendel, V., Ruellan, E., Okino, K., Escartin, J., et al. (2006). Modes of seafloor generation at a melt-poor ultraslow-spreading ridge. *Geology*, *34*(7), 605–608. https://doi.org/10.1130/G22486.1
Dannowski, A., Grevemeyer, I., Ranero, C. R., Ceuleneer, G., Maia, M., Morgan, J. P., & Gente, P. (2010). Seismic structure of an oceanic core complex at the Mid-Atlantic Ridge, 22°19′N. *Journal of Geophysical Research*, *115*(B7), B07106. https://doi.org/10.1029/2009JB006943
de Brito, A. (2019). Mélange mécanique et métamorphisme des lithologies basiques et ultrabasiques au cours de la mylonitisation dans le système transformant de St. Paul, Dorsale Médio-Atlantique (Doctoral dissertation, Brest).
DeMets, C., Gordon, R. G., & Argus, D. F. (2010). Geologically current plate motions. *Geophysical Journal International*, *181*(1), 1–80. https://doi.org/10.1111/j.1365-246X.2009.04491.x
DeMets, C., & Merkouriev, S. (2019). High-resolution reconstructions of South America plate motion relative to Africa, Antarctica and North America: 34 Ma to present. *Geophysical Journal International*, *217*(3), 1821–1853. https://doi.org/10.1093/gji/ggz087
Dick, H. J. B., Tivey, M. A., & Tucholke, B. E. (2008). Plutonic foundation of a slow-spreading ridge segment: Oceanic core complex at Kane Megamullion, 23°30′N, 45°20′W. *Geochemistry, Geophysics, Geosystems*, *9*(5), Q05014. https://doi.org/10.1029/2007GC001645
D'Orazio, M., Boschi, C., & Brunelli, D. (2004). Talc-rich hydrothermal rocks from the St. Paul and Conrad fracture zones in the Atlantic Ocean. *European Journal of Mineralogy*, *16*(1), 73–83. https://doi.org/10.1127/0935-1221/2004/0016-0073
Escartín, J., John, B., Cannat, M., Olive, J. A., Cheadle, M., Früh-Green, G., & Cotterill, C. (2022). Tectonic termination of oceanic detachment faults, with constraints on tectonic uplift and mass wasting related erosion rates. *Earth and Planetary Science Letters*, *584*, 117449. https://doi.org/10.1016/j.epsl.2022.117449
Escartín, J., Mével, C., Petersen, S., Bonnemains, D., Cannat, M., Andreani, M., et al. (2017). Tectonic structure, evolution, and the nature of oceanic core complexes and their detachment fault zones (13°20′N and 13°30′N, Mid Atlantic Ridge). *Geochemistry, Geophysics, Geosystems*, *18*(4), 1451–1482. https://doi.org/10.1002/2016GC006775
Escartín, J., Smith, D. K., Cann, J., Schouten, H., Langmuir, C. H., & Escrig, S. (2008). Central role of detachment faults in accretion of slow-spreading oceanic lithosphere. *Nature*, *455*(7214), 790–794. https://doi.org/10.1038/nature07333
Esperança, S., Sichel, S. E., Horan, R. J., Walker, M. F., Juteau, T., & Hekinian, R. (1999). Some abyssal peridotites from cold oceanic lithosphere are old. In *9th annual V. M. Goldsmidt conference LPI contribution* (Vol. 971, p. 81).
Gasperini, L., Bonatti, E., Brunelli, D., Carrara, G., Cipriani, A., Fabretti, P., et al. (1997). New data on the geology of the Romanche F.Z., equatorial Atlantic: PRIMAR-96 cruise report. *Giornale di Geologia*, *59*(1–2), 3–18.

Hayman, N. W., Grindlay, N. R., Perfit, M. R., Mann, P., Leroy, S., & de Lépinay, B. M. (2011). Oceanic core complex development at the ultraslow spreading Mid-Cayman Spreading Center. *Geochemistry, Geophysics, Geosystems*, *12*(3), Q0AG02. https://doi.org/10.1029/2010gc003240
Hekinian, R., & Juteau, T. (1997). Saint Paul cruise. *RV Le Nadir*. https://doi.org/10.17600/97080050
Hekinian, R., Juteau, T., Gràcia, E., Sichler, B., Sichel, S., Udintsev, G., et al. (2000). Submersible observations of equatorial Atlantic mantle: The St. Paul Fracture Zone region. *Marine Geophysical Researches*, *21*(6), 529–560. https://doi.org/10.1023/A:1004819701870
Ildefonse, B., Blackman, D. K., John, B. E., Ohara, Y., Miller, D. J., MacLeod, C. J., et al. (2007). Oceanic core complexes and crustal accretion at slow-speading ridges. *Geology*, *35*(7), 623–626. https://doi.org/10.1130/G23531A.1
Lagabrielle, Y., Bideau, D., Cannat, M., Karson, J. A., & Mével, C. (1998). Ultramafic-mafic plutonic rock suites exposed along the mid-Atlantic ridge (10°N-30°N). Symmetrical-asymmetrical distribution and implications for seafloor spreading processes. In *Geophysical monograph series* (Vol. 106, pp. 153–176). Blackwell Publishing Ltd. https://doi.org/10.1029/GM106p0153
Lavier, L. L., Buck, W. R., & Poliakov, A. N. B. (1999). Self-consistent rolling-hinge model for the evolution of large-offset low-angle normal faults. *Geology*, *27*(12), 1127–1130. https://doi.org/10.1130/0091-7613(1999)027<1127:SCRHMF>2.3.CO;2
Lavier, L. L., Buck, W. R., & Poliakov, A. N. B. (2000). Factors controlling normal fault offset in an ideal brittle layer. *Journal of Geophysical Research*, *105*(B10), 23431–23442. https://doi.org/10.1029/2000jb900108
Le Voyer, M., Cottrell, E., Kelley, K. A., Brounce, M., & Hauri, E. H. (2015). The effect of primary versus secondary processes on the volatile content of MORB glasses: An example from the equatorial Mid-Atlantic Ridge (5°N–3°S). *Journal of Geophysical Research: Solid Earth*, *120*(1), 125–144. https://doi.org/10.1002/2014JB011160
Ligi, M., Bonatti, E., Cipriani, A., & Ottolini, L. (2005). Water-rich basalts at mid-ocean-ridge cold spots. *Nature*, *434*(7029), 66–69. https://doi.org/10.1038/nature03264
Ligi, M., Bonatti, E., Gasperini, L., & Poliakov, A. N. B. (2002). Oceanic broad multifault transform plate boundaries. *Geology*, *30*(1), 11–14. https://doi.org/10.1130/0091-7613(2002)030<0011:OBMTPB>2.0.CO;2
Ligi, M., Cuffaro, M., Chierici, F., & Calafato, A. (2008). Three-dimensional passive mantle flow beneath mid-ocean ridges: An analytical approach. *Geophysical Journal International*, *175*(2), 783–805. https://doi.org/10.1111/j.1365-246X.2008.03931.x
MacLeod, C. J., Escartin, J., Banerji, D., Banks, G. J., Gleeson, M., Irving, D. H. B., et al. (2002). Direct geological evidence for oceanic detachment faulting: The Mid-Atlantic Ridge, 15°45′N. *Geology*, *30*(10), 879–882. https://doi.org/10.1130/0091-7613(2002)030<0879:DGEFOD>2.0.CO;2
MacLeod, C. J., Searle, R. C., Murton, B. J., Casey, J. F., Mallows, C., Unsworth, S. C., et al. (2009). Life cycle of oceanic core complexes. *Earth and Planetary Science Letters*, *287*(3–4), 333–344. https://doi.org/10.1016/j.epsl.2009.08.016
Maia, M. (2013). COLMEIA cruise, RV L'Atalante (SISMER, 2013). https://doi.org/10.17600/13010010
Maia, M., & Arkani-Hamed, J. (2002). The support mechanism of the young Foundation Seamounts inferred from bathymetry and gravity. *Geophysical Journal International*, *149*(1), 190–210. https://doi.org/10.1046/j.1365-246X.2002.01635.x
Maia, M., Birot, D., Brachet, C., Brehme, I., Briais, A., Brunelli, D., et al. (2014). Preliminary report on the COLMEIA Cruise, Equatorial Atlantic Recife, January 24 -Recife, February 28, 2013. *InterRidge Newsletter*, *22*, 52–56.
Maia, M., Mougel, B., Hémond, C., Briais, A., Brachet, C., Konn, C., et al. (2017). *Campagne COLMEIA "COLd mantle exhumation and intra-transform accretion"*. Rapport de campagne océanographique. CNRS-UMR 6538 Domaines Océaniques. ⟨hal-03888652⟩.
Maia, M., Sichel, S., Briais, A., Brunelli, D., Ligi, M., Ferreira, N., et al. (2016). Extreme mantle uplift and exhumation along a transpressive transform fault. *Nature Geoscience*, *9*(8), 619–623. https://doi.org/10.1038/ngeo2759
Maia, M., Vincent, C., Briais, A., & Ligi, M. (2023). Gridded geophysical shipboard data on the South Intra-Transform segment of the St. Paul transform system (COLMEIA cruise) [Dataset]. SEANOE. https://doi.org/10.17882/92690
Manatschal, G., Sauter, D., Karpoff, A. M., Masini, E., Mohn, G., & Lagabrielle, Y. (2011). The Chenaillet Ophiolite in the French/Italian Alps: An ancient analogue for an oceanic core complex? *Lithos*, *124*(3–4), 169–184. https://doi.org/10.1016/j.lithos.2010.10.017
Morgan, J. P., & Forsyth, D. W. (1988). Three-dimensional flow and temperature perturbations due to a transform offset: Effects on oceanic crustal and upper mantle structure. *Journal of Geophysical Research*, *93*(B4), 2955. https://doi.org/10.1029/JB093iB04p02955
Ohara, Y., Yoshida, T., Kato, Y., & Kasuga, S. (2001). Giant megamullion in the Parece Vela backarc basin. *Marine Geophysical Researches*, *22*(1), 47–61. https://doi.org/10.1023/a:1004818225642
Okino, K., Matsuda, K., Christie, D. M., Nogi, Y., & Koizumi, K. (2004). Development of oceanic detachment and asymmetric spreading at the Australian-Antarctic Discordance. *Geochemistry, Geophysics, Geosystems*, *5*(12), Q12012. https://doi.org/10.1029/2004GC000793
Olive, J. A., Behn, M. D., & Tucholke, B. E. (2010). The structure of oceanic core complexes controlled by the depth distribution of magma emplacement. *Nature Geoscience*, *3*(7), 491–495. https://doi.org/10.1038/ngeo888
Olive, J. A., & Dublanchet, P. (2020). Controls on the magmatic fraction of extension at mid-ocean ridges. *Earth and Planetary Science Letters*, *549*, 116541. https://doi.org/10.1016/J.EPSL.2020.116541
Parnell-Turner, R., Escartín, J., Olive, J. A., Smith, D. K., & Petersen, S. (2018). Genesis of corrugated fault surfaces by strain localization recorded at oceanic detachments. *Earth and Planetary Science Letters*, *498*, 116–128. https://doi.org/10.1016/J.EPSL.2018.06.034
Parsons, B., & Sclater, J. G. (1977). An analysis of the variation of ocean floor bathymetry and heat flow with age. *Journal of Geophysical Research*, *82*(5), 803–827. https://doi.org/10.1029/jb082i005p00803
Planert, L., Flueh, E. R., Tilmann, F., Grevemeyer, I., & Reston, T. J. (2010). Crustal structure of a rifted oceanic core complex and its conjugate side at the MAR at 5°S: Implications for melt extraction during detachment faulting and core complex formation. *Geophysical Journal International*, *181*(1), 113–126. https://doi.org/10.1111/j.1365-246X.2010.04504.x
Poncelet, C., Billant, G., & Corre, M.-P. (2022). Globe (GLobal oceanographic bathymetry explorer) software. *SEANOE*. https://doi.org/10.17882/70460
QGIS.org. (2022). *QGIS geographic information system*. QGIS Association. Retrieved from http://www.qgis.org
Reston, T. J. (2018). Flipping detachments: The kinematics of ultraslow spreading ridges. *Earth and Planetary Science Letters*, *503*, 144–157. https://doi.org/10.1016/J.EPSL.2018.09.032
Reston, T. J., & Ranero, C. R. (2011). The 3-D geometry of detachment faulting at mid-ocean ridges. *Geochemistry, Geophysics, Geosystems*, *12*(7), 1–19. https://doi.org/10.1029/2011GC003666
Reston, T. J., Weinrebe, W., Grevemeyer, I., Flueh, E. R., Mitchell, N. C., Kirstein, L., et al. (2002). A rifted inside corner massif on the Mid-Atlantic Ridge at 5°S. *Earth and Planetary Science Letters*, *200*(3–4), 255–269. https://doi.org/10.1016/S0012-821X(02)00636-2
Sandwell, D. T., Müller, R. D., Smith, W. H. F., Garcia, E., & Francis, R. (2014). New global marine gravity model from CryoSat-2 and Jason-1 reveals buried tectonic structure. *Science*, *346*(6205), 65–67. https://doi.org/10.1126/science.1258213
Sauter, D., Cannat, M., Rouméjon, S., Andreani, M., Birot, D., Bronner, A., et al. (2013). Continuous exhumation of mantle-derived rocks at the Southwest Indian Ridge for 11 million years. *Nature Geoscience*, *6*(4), 314–320. https://doi.org/10.1038/ngeo1771

Schilling, J. G., Hanan, B. B., McCully, B., Kingsley, R. H., & Fontignie, D. (1994). Influence of the Sierra Leone mantle plume on the equatorial Mid-Atlantic Ridge: A Nd-Sr-Pb isotopic study. *Journal of Geophysical Research*, *99*(B6), 12005–12028. https://doi.org/10.1029/94jb00337

Schilling, J. G., Ruppel, C., Davis, A. N., McCully, B., Tighe, S. A., Kingsley, R. H., & Lin, J. (1995). Thermal structure of the mantle beneath the equatorial Mid-Atlantic Ridge: Inferences from the spatial variation of dredged basalt glass compositions. *Journal of Geophysical Research*, *100*(B6), 10057–10076. https://doi.org/10.1029/95JB00668

Schoolmeesters, N., Cheadle, M. J., John, B. E., Reiners, P. W., Gee, J., & Grimes, C. B. (2012). The cooling history and the depth of detachment faulting at the Atlantis Massif oceanic core complex. *Geochemistry, Geophysics, Geosystems*, *13*(10), Q0AG12. https://doi.org/10.1029/2012gc004314

Schroeder, T., Cheadle, M. J., Dick, H. J. B., Faul, U., Casey, J. F., & Kelemen, P. B. (2007). Nonvolcanic seafloor spreading and corner-flow rotation accommodated by extensional faulting at 15°N on the Mid-Atlantic Ridge: A structural synthesis of ODP Leg 209. *Geochemistry, Geophysics, Geosystems*, *8*(6), Q06015. https://doi.org/10.1029/2006GC001567

Seyler, M., & Bonatti, E. (1997). Regional-scale melt-rock interaction in lherzolitic mantle in the Romanche Fracture Zone (Atlantic Ocean). *Earth and Planetary Science Letters*, *146*(1–2), 273–287. https://doi.org/10.1016/s0012-821x(96)00220-8

Sichel, S. E., Esperança, S., Motoki, A., Maia, M., Horan, M. F., Szatmari, P., et al. (2008). Geophysical and geochemical evidence for cold upper mantle beneath the Equatorial Atlantic Ocean. *Revista Brasileira de Geofísica*, *26*(1), 69–86. https://doi.org/10.1590/S0102-261X2008000100006

Sichler, B., & Hékinian, R. (2002). Three-dimensional inversion of marine magnetic anomalies on the equatorial Atlantic Ridge (St. Paul Fracture Zone): Delayed magnetization in a magmatically starved spreading center? *Journal of Geophysical Research*, *107*(B12), EPM7–1. https://doi.org/10.1029/2001JB000401

Smith, D. K., Cann, J. R., & Escartín, J. (2006). Widespread active detachment faulting and core complex formation near 13°N on the Mid-Atlantic Ridge. *Nature*, *442*(7101), 440–443. https://doi.org/10.1038/nature04950

Smith, D. K., Escartín, J., Schouten, H., & Cann, J. R. (2008). Fault rotation and core complex formation: Significant processes in seafloor formation at slow-spreading mid-ocean ridges (Mid-Atlantic Ridge, 13°–15°N). *Geochemistry, Geophysics, Geosystems*, *9*(3), Q03003. https://doi.org/10.1029/2007GC001699

Smith, W. H., & Sandwell, D. T. (1994). Bathymetric prediction from dense satellite altimetry and sparse shipboard bathymetry. *Journal of Geophysical Research*, *99*(B11), 21803–21824. https://doi.org/10.1029/94jb00988

Spencer, J. E. (1999). Geologic continuous casting below continental and deep-sea detachment faults and at the striated extrusion of Sacsayhuaman, Peru. *Geology*, *27*(4), 327–330. https://doi.org/10.1130/0091-7613(1999)027<0327:GCCBCA>2.3.CO;2

Spencer, J. E., & Ohara, Y. (2008). Magmatic and tectonic continuous casting in the circum-Pacific region. *Circum-Pacific Tectonics, Geologic Evolution, and Ore Deposits*, 1–24.

Spencer, J. E., & Ohara, Y. (2014). Curved grooves at the Godzilla Megamullion in the Philippine Sea and their tectonic significance. *Tectonics*, *33*(6), 1028–1038. https://doi.org/10.1002/2013TC003515

Stein, C. A., & Stein, S. (1992). A model for the global variation in oceanic depth and heat flow with lithospheric age. *Nature*, *359*(6391), 123–129. https://doi.org/10.1038/359123a0

Tani, K., Dunkley, D. J., & Ohara, Y. (2011). Termination of backarc spreading: Zircon dating of a giant oceanic core complex. *Geology*, *39*(1), 47–50. https://doi.org/10.1130/g31322.1

Tenzer, R., & Gladkikh, V. (2014). Assessment of density variations of marine sediments with ocean and sediment depths. *The Scientific World Journal*, *2014*, 1–9. https://doi.org/10.1155/2014/823296

Thibaud, R., Gente, P., & Maia, M. (1998). A systematic analysis of the Mid-Atlantic Ridge morphology and gravity between 15°N and 40°N: Constraints of the thermal structure. *Journal of Geophysical Research*, *103*(10), 24223–24243. https://doi.org/10.1029/97jb02934

Tucholke, B. E. (1992). Massive submarine rockslide in the rift-valley wall of the Mid-Atlantic Ridge. *Geology*, *20*(2), 129–132. https://doi.org/10.1130/0091-7613(1992)020<0129:MSRITR>2.3.CO;2

Tucholke, B. E., Behn, M. D., Buck, W. R., & Lin, J. (2008). Role of melt supply in oceanic detachment faulting and formation of megamullions. *Geology*, *36*(6), 455–458. https://doi.org/10.1130/G24639A.1

Tucholke, B. E., Lin, J., & Kleinrock, M. C. (1998). Megamullions and mullion structure defining oceanic metamorphic core complexes on the Mid-Atlantic Ridge. *Journal of Geophysical Research*, *103*(5), 9857–9866. https://doi.org/10.1029/98jb00167

Udintsev, G. B. (1996). Equatorial segment of the Mid-Atlantic Ridge. In *IOC technical series* (Vol. 46). UNESCO.

Wagner, T. (2002). Late Cretaceous to early Quaternary organic sedimentation in the eastern Equatorial Atlantic. *Palaeogeography, Palaeoclimatology, Palaeoecology*, *179*(1–2), 113–147. https://doi.org/10.1016/S0031-0182(01)00415-1

References From the Supporting Information

Blackman, D. K., & Forsyth, D. W. (1992). *The effects of plate thickening on three-dimensional, passive flow of the mantle beneath mid-ocean ridges* (Vol. 71, pp. 311–326). Washington DC American Geophysical Union Geophysical Monograph Series.

Cande, S. C., LaBrecque, J. L., & Haxby, W. F. (1988). Plate kinematics of the South Atlantic: Chron C34 to present. *Journal of Geophysical Research*, *93*(B11), 13479–13492. https://doi.org/10.1029/jb093ib11p13479

Grevemeyer, I., Rüpke, L. H., Morgan, J. P., Iyer, K., & Devey, C. W. (2021). Extensional tectonics and two-stage crustal accretion at oceanic transform faults. *Nature*, *591*(7850), 402–407. https://doi.org/10.1038/s41586-021-03278-9

Maia, M. (2019). Topographic and morphologic evidences of deformation at oceanic transform faults: Far-field and local-field stresses. In *Transform plate boundaries and fracture zones* (pp. 61–87). Elsevier.

Prince, R. A., & Forsyth, D. W. (1988). Horizontal extent of anomalously thin crust near the Vema fracture zone from the three-dimensional analysis of gravity anomalies. *Journal of Geophysical Research*, *93*(B7), 8051–8063. https://doi.org/10.1029/jb093ib07p08051

Rommevaux, C., Deplus, C., Patriat, P., & Sempéré, J. C. (1994). Three-dimensional gravity study of the Mid-Atlantic Ridge: Evolution of the segmentation between 28 and 29N during the last 10 my. *Journal of Geophysical Research*, *99*(B2), 3015–3029. https://doi.org/10.1029/93jb02361

Shaw, P. R., & Cande, S. C. (1990). High-resolution inversion for South Atlantic Plate kinematics using joint altimeter and magnetic anomaly data. *Journal of Geophysical Research*, *95*(B3), 2625–2644. https://doi.org/10.1029/JB095IB03P02625